

The Journal of Neuroscience

<http://jneurosci.msubmit.net>

JN-RM-5729-12R2

Input-output features of anatomically-identified CA3 neurons during hippocampal sharp wave/ripple oscillation in vitro.

Norbert Hajos, Institute of Experimental Medicine of the Hungarian Academy of Sciences Maria Karlocai, Institute of Experimental Medicine of the Hungarian Academy of Sciences Beata Nemeth, Institute of Experimental Medicine of the Hungarian Academy of Sciences Istvan Ulbert, MTA Hannah Monyer, University Hospital of Neurology Gabor Szabo, Institute of Experimental Medicine, Hungarian Academy of Sciences Ferenc Erdelyi, Institute of Experimental Medicine, Hungarian Academy of Sciences Tamas Freund, Inst. Exp. Med., Budapest Attila Gulyas, Institute of Experimental Medicine

Commercial Interest: No

Input-output features of anatomically-identified CA3 neurons during hippocampal sharp wave/ripple oscillation *in vitro*.

Norbert Hájos^{1*}, Mária R. Karlócai^{1*}, Beáta Németh¹, István Ulbert^{2,3}, Hannah Monyer⁴, Gábor Szabó¹, Ferenc Erdélyi¹, Tamás F. Freund^{1,2} and Attila I. Gulyás¹

¹Institute of Experimental Medicine, Hungarian Academy of Sciences, H-1083 Budapest, Hungary

²Péter Pázmány Catholic University, Faculty of Information Technology, H-1088, Budapest, Hungary

³Institute of Cognitive Neuroscience and Psychology, Research Centre for Natural Sciences, Hungarian Academy of Sciences, H-1025, Budapest, Hungary

⁴Department of Clinical Neurobiology, University Hospital of Neurology, 69120 Heidelberg, Germany

*These authors contributed equally to this study.

Abbreviated title: Spiking and synaptic currents during sharp waves.

Number of pages: 31

Number of figures: 8

Number of tables: 3

Number of words for Abstract: 230

Number of words for Introduction: 500

Number of words for Discussion: 1498

Correspondence:

Norbert Hájos

Institute of Experimental Medicine

Hungarian Academy of Sciences

Budapest, H-1450, Hungary

Phone: 36-12109400/387

Fax: 36-1-2109412

Email: hajos@koki.hu

Acknowledgements This work was supported by the Wellcome Trust International Senior Research Fellowship, the National Office for Research and Technology (OMFB-01678/2009), the Hungarian Scientific Research Fund (NNF 78917, NNF 85659, OTKA K83251, OTKA K81354), French-Hungarian grants ANR-TÉT Neurogen, ANR-TÉT Multisca and TÁMOP-4.2.1.B-11/2/KMR-2011-0002. We thank Dr. Szabolcs Káli for his comments, Erzsébet Gregori for her excellent technical assistance and Dr. Gergely Szabó for providing some data.

Abstract

Hippocampal sharp waves and the associated ripple oscillations (SWRs) are implicated in memory processes. These network events emerge intrinsically in CA3 network. To understand cellular interactions that generate SWRs, we detected first spiking activity followed by recording of synaptic currents in distinct types of anatomically-identified CA3 neurons during SWRs that occurred spontaneously in mouse hippocampal slices. We observed that the vast majority of interneurons fired during SWRs, while only a small portion of pyramidal cells was found to spike. There were substantial differences in the firing behavior among interneuron groups; parvalbumin-expressing basket cells were one of the most active GABAergic cells during SWRs, while ivy cells were silent. Analysis of the synaptic currents during SWRs uncovered that the dominant synaptic input to pyramidal cell was inhibitory, whereas spiking interneurons received larger synaptic excitation than inhibition. The discharge of all interneurons was primarily determined by the magnitude and the timing of synaptic excitation. Strikingly, we observed that the temporal structure of synaptic excitation and inhibition during SWRs significantly differed between parvalbumin-containing basket cells, axo-axonic cells and CB1-expressing basket cells, which might explain their distinct recruitment to these synchronous events. Our data support the hypothesis that the active current sources restricted to the stratum pyramidale during SWRs originate from the synaptic output of parvalbumin-expressing basket cells. Thus, in addition to gamma oscillation, these GABAergic cells play a central role in SWR generation.

Introduction

Sharp wave-associated ripple oscillations (SWRs), which reflect fast synchronous network activity at 150-200 Hz, decorate the hippocampal electro-encephalogram recorded during both awake immobility and sleep (Buzsáki, 1986). These events have been suggested to be associated with memory consolidation (Buzsáki, 1989). In support of this suggestion, recent studies showed that selective disruption of SWRs during post-training consolidation periods impairs hippocampus-dependent memory (Girardeau et al., 2009; Jadhav et al., 2012). SWRs are thought to reflect the flow of information from area CA3 to CA1 within the hippocampus as well as between the hippocampus and its output structures, where they significantly modulate the spiking activity of local neurons (Chrobak and Buzsáki, 1996; Dragoi et al., 1999; Logothetis et al., 2012). In spite of extensive investigations of SWRs *in vivo*, the network mechanisms underlying the generation of these population events remain largely unknown.

Though SWRs can be recorded from both CA3 and CA1, it has been shown that they are generated in CA3 and are only transmitted to CA1 (Csicsvari et al., 2000; Nakashiba et al., 2009). There is no ‘wave-by-wave’ transfer of ripples from the CA3 region to CA1, only the SWR envelop is coincident (Sullivan et al., 2011). *In vivo* data showed that on average the activity of both pyramidal cells and interneurons increases during SWRs, and it is hypothesized that both neuron types are necessary for the generation of this population activity (Csicsvari et al., 2000). To date, however, the activity of only a limited number of anatomically-identified hippocampal interneurons has been correlated with SWRs (Klausberger and Somogyi, 2008). Importantly, these recordings were almost exclusively done in CA1 that does not generate SWRs independently, but inherits these population events from CA3.

To clarify the synaptic mechanisms underlying the SWR generation, *in vitro* models of these population events have been introduced (Kubota et al., 2003; Maier et al., 2003; Behrens et al., 2005; Wu et al., 2005; de la Prida et al., 2006). This network activity has been shown to emerge spontaneously in mouse hippocampal slices, or could be induced by increasing the excitability of neurons in rat slices. As in the intact brain, SWRs recorded in hippocampal slices were found to be initiated by neuronal ensembles in CA3, and then propagate to CA1. Moreover, it was shown *in vitro* that both excitatory and inhibitory synaptic transmission was necessary for the generation of SWRs, and only a small proportion

of pyramidal cells was active during these network events similar to what was found *in vivo* (Csicsvari et al., 2000; Le Van Quyen et al., 2008).

To reveal the mechanism of SWR generation, we aimed to uncover the firing properties of different types of anatomically-identified neurons in CA3 during spontaneously occurring SWRs in mouse hippocampal slices. By relating the synaptic currents to the spiking of individual neurons we found that the distinct synaptic input in different neurons during SWRs could at least partially explain their different spiking behavior. In addition, our results propose a central role for parvalbumin-containing basket cells in SWR generation.

Methods

Animals were kept and used according to the regulations of the European Community's Council Directive of 24 November 1986 (86/609/EEC), and experimental procedures were reviewed and approved by the Animal Welfare Committee of the Institute of Experimental Medicine, Hungarian Academy of Sciences, Budapest.

CD1 mice of both sexes (postnatal day 17-29) were used in most of the experiments unless is specified. To measure selectively from cells containing the Ca^{2+} binding protein parvalbumin (PV), transgenic mice expressing the enhanced green fluorescent protein (eGFP) controlled by PV promoter (Meyer et al., 2002) were also used in this study (postnatal day 18-25). Cholecystokinin/CB1 cannabinoid receptor expressing interneurons were sampled in slices prepared from GAD65-EGFP transgenic mice (postnatal day 19-23) (Lopez-Bendito et al., 2004). In all cases, the mice were decapitated under deep isoflurane anaesthesia. The brain was removed into ice cold cutting solution, which had been bubbled with 95% O_2 -5% CO_2 (carbogen gas) for at least 30 minutes before use. The cutting solution contained (in mM): 205 sucrose, 2.5 KCl, 26 NaHCO_3 , 0.5 CaCl_2 , 5 MgCl_2 , 1.25 NaH_2PO_4 , 10 glucose, saturated with 95% O_2 -5% CO_2 . Horizontal hippocampal slices of 400-500 μm thickness were cut using a vibratome (Leica VT1000S or VT1200S, Wetzlar, Germany).

After acute slice preparation the slices were placed into an interface-type holding chamber for recovery. This chamber contained standard aCSF at 35°C that gradually cooled down to room temperature. The aCSF had the following composition (in mM): 126 NaCl, 2.5 KCl, 26 NaHCO_3 , 2 CaCl_2 , 2 MgCl_2 , 1.25 NaH_2PO_4 , 10 glucose, saturated with 95% O_2 -5% CO_2 . After incubation for at least one hour, slices were transferred individually into a submerged-style recording chamber equipped with a dual superfusion system for improved metabolic supply to the slices (Hajos et al., 2009). In this design, the slices were placed on a

metal mesh and two separate fluid inlets allowed aCSF to flow both above and below the slices with a rate of 3-3.5 ml/min for each flow channel at 30-32 °C (Supertech Instruments Ltd., Pecs, Hungary).

Standard patch electrodes were used in all recording configurations (i.e. in whole-cell patch-clamp, loose-patch and field potential recordings). Pipette resistances were 3-6 MΩ when filled either with the intrapipette solution or with aCSF. The intrapipette solution contained (in mM): 138 K-gluconate, 3 CsCl, 10 disodium creatine phosphate, 4 Mg-ATP, 0.4 Tris-GTP, 10 HEPES, 0.2 QX 314; pH: 7.38; 285 mOsm^l⁻¹. For later morphological identification of the recorded cells biocytin in a concentration of 3-5 mg/ml was added to the pipette solution freshly before use.

Extracellular recordings and current source density calculation. The local field potential (LFP) was recorded with a laminar multielectrode array (24 channels, 50 μm inter-contact distance, Neuronelektród Ltd., Budapest, Hungary) using a custom made referential amplifier system (band-pass from 0.1 Hz to 7 kHz)(Ulbert et al., 2001). Signals were digitized with a 16 bit resolution analog-to-digital converter (National Instruments, Austin TX, USA) and recorded at 20 kHz sampling rate on each channel, using a custom made virtual instrument in LabView (National Instruments, Austin TX, USA). The laminar multielectrode array was placed on the surface of the hippocampal slice perpendicularly to the pyramidal cell layer. In this way the entire region was covered by the array so that extracellular recordings were made from each hippocampal layer. Current source density (CSD) calculations were made using the three-point formula smoothed by Hamming window (Ulbert et al. 2001). Results are depicted on heat map using custom made software.

Data acquisition. All other data were recorded with a Multiclamp 700B amplifier (Molecular Devices, Sunnyvale, CA.). As a first step, two pipettes filled with aCSF were used. Local field potentials were monitored with a pipette placed into the stratum pyramidale of the CA3 area, while another pipette was used to concomitantly record the firing activity of individual neurons in the CA3 region. The loose-patch recordings of the neuronal discharge were visually guided using differential interference contrast microscopy (Olympus BX61W) for 2-5 minutes, depending on the firing frequency of the cell. This pipette was then withdrawn from the slice, and whole-cell patch-clamp recordings were performed on the same cells with another pipette filled with intrapipette solution. Access resistance was in the range of 5-20 MOhm. Only recordings, where the access resistance did not change substantially (more than

25%), were included in the study. Reported values of voltage measurements were not corrected for the junction potential. To record excitatory postsynaptic currents (EPSCs) and inhibitory postsynaptic currents (IPSCs), cells were voltage clamped at a holding potential of the estimated reversal potential for IPSCs (~ -80 mV) and EPSCs (~ 0 mV), respectively. Both field and unit recordings were low-pass filtered at 3 kHz using the built-in Bessel filter of the amplifier. Data were digitized at 10 kHz with a PCI-6042E board (National Instruments, Austin, Texas) using EVAN 1.3 software (courtesy of Prof. Istvan Mody, UCLA, CA), and were analyzed offline with custom-made programs written in MATLAB 7.0.4 and Delphi (by A.I.G.).

Digital signal processing and analysis. Signals were filtered with a two-way RC filter to preserve phase. All automatic detection steps were supervised. Spike detection in loose-patch recordings was done on 500 Hz-high-pass-filtered traces using a threshold value of 6 times the standard deviation of the signal. SWRs were pre-detected on 30 Hz-low-pass-filtered field recordings using a threshold value of 4 times the standard deviation of the signal. The pre-detected SWRs were then re-detected using a program that measured various SWR features and eliminated recording artifacts similar to SWRs. Namely, on the low-pass-filtered signal the program measured: 1) peak amplitude and peak time of SWRs, 2) duration of the SWR positive phase crossing 3 times standard deviation, 3) amplitude, time and half decay of the negativity following the SWRs. On a ripple band-pass-filtered trace (170-200 Hz) the program also detected 4) the time of ripple negative peaks and taking the absolute value of the ripple band-passed signal and low-pass filtering it calculated 5) the ripple power peak, time and area. The same program calculated the number of spikes of the recorded neuron during each SWR; and assigned to each spike a time relative to SWR peak and a phase relative to ripple negativities. The algorithm did not assign a phase to a spike when it was not between two subsequent ripple negativities. Circular statistics were then used to calculate average ripple phase and the strength of the coupling. Ripple frequency was calculated by Fast Fourier transformation or by calculating the characteristic ripple negativity inter-event interval, both measurement put the ripple frequency around 184 Hz (see the text).

Synaptic currents during SWRs were calculated in flexible windows set by the width of the actual SWR. Synaptic conductances were calculated by dividing the current values with the difference of the holding potential and the experimentally determined reversal potential for the measured current for each cell using

$$g_{e/i} = \frac{I_{e/i}}{(V_h - E_{e/i}^{rev})} \quad (1)$$

where $I_{e/i}$ is the phasic excitatory/inhibitory current, V_h is the holding potential, and $E_{e/i}^{rev}$ is the reversal potential for the conductance of interest. The conductances were used to estimate the net apparent reversal potential (E_{syn}^{rev}) by solving

$$I_{syn} = g_e (E_{syn}^{rev} - E_e^{rev}) + g_i (E_{syn}^{rev} - E_i^{rev}) = 0$$

$$\Rightarrow E_{syn}^{rev} = \frac{g_e E_e^{rev} + g_i E_i^{rev}}{g_e + g_i} \quad (2)$$

To calculate averages we identified the ripple cycle closest to the SWR peak and used its negative peak as triggering event for correlations.

Anatomical identification of the neurons. The recorded cells were filled with biocytin during the recordings. After the recording the slices were fixed in 4 % paraformaldehyde in 0.1 M phosphate buffer (PB; pH=7.4) for at least 1 hour, followed by washout with PB several times and incubation in 30 % sucrose in 0.1 M PB for at least 2 hours. Then slices were freeze-thawed three times above liquid nitrogen and treated with 1 % H₂O₂ in PB for 15 minutes to reduce the endogenous peroxidase activity. Recorded cells were visualised using avidin-biotinylated horseradish peroxidase complex reaction (Vector Laboratories Inc., Burlingame, CA) with nickel-intensified 3,3'-diaminobenzidine as chromogen giving a dark reaction product. After dehydration and embedding in Durcupan cells were morphologically identified on the basis of their dendritic and axonal arborisation. Representative neurons were reconstructed using a drawing tube.

Separation of basket and axo-axonic cells. To distinguish basket cells and axo-axonic cells, slices were re-sliced to 40 µm thick sections and processed for immunofluorescence double labeling. Ankyrin G-immunostaining was applied together with biocytin visualization as described before (Gulyas et al., 2010). In our earlier studies, we validated this light microscopic identification of axo-axonic and basket cells by electron microscopy (Gulyás et

al., 2010). Briefly, sections were treated with 0.2 mg/ml pepsin (Dako, Glostrup, Denmark) in 0.2 M HCl at 37°C for 15 min and were washed in 0.1 M PB. Non-specific binding sites were blocked in 10% normal goat serum (Vector) in TBS (pH 7.4), followed by incubation with a mouse anti-ankyrin G antibody (1:100, Santa Cruz Biotechnology, CA) diluted in TBS containing 2% NGS and 0.05% Triton X-100 for 72 hours at 4 °C. Following several washes in TBS, Alexa594-conjugated goat anti-mouse (1:200; Life Technologies, NY) was used to visualize the ankyrin G-immunostaining, and Alexa488-conjugated streptavidin (1:500; Life Technologies) was used to label biocytin. Sections were then mounted on slides in Vectashield (Vector Laboratories). The staining was analyzed and images were taken by using an AxioImager.Z1 microscope (Zeiss, Germany). Subsequently, representative basket and axo-axonic cells were further developed by immunoperoxidase reaction using DAB-Ni for anatomical reconstruction.

Statistical comparisons. As the first step, we compared the data obtained in pyramidal cells with those recorded in all interneurons. Next, we compared data in the two groups of functionally distinct interneuron types, the perisomatic region-targeting interneurons (including parvalbumin-containing basket cells, axo-axonic cells and CB1-expressing basket cells) and dendritic layer-innervating interneurons (including OLM cells, oriens-oriens cells, oriens-radiatum cells, and radiatum cells). Finally, we evaluated the statistical difference among cell types within the perisomatic region targeting-interneurons or within the group of dendritic layer-innervating interneurons. If the results were taken from a normal distribution based on a normality test, t-test and ANOVA followed by Fisher post hoc test were used for comparison of two groups and multiple groups, respectively. If the normality test rejected the hypothesis that the results were taken from a normal distribution, Mann-Whitney (M-W) test and Kruskal-Wallis (K-W) ANOVA were used for comparison of two groups and multiple groups, respectively. To correlate normally distributed linear-linear variables the Pearson's correlation coefficient was used, and the results are quoted as R. Statistica version 11 (Stat Soft, Inc, Tulsa, OK, USA) and OriginPro 8.6 (Nothampton, MA) was used, data are presented as mean ± SEM,), unless stated otherwise.

The Rayleigh probability (p_r) was used to determine the significance of the phase-coupling. It was calculated by the following equation:

$$p_r = e^{-\frac{1}{2}} \left(1 + \frac{2E - E^2}{4n} - \frac{24E - 192E^2 + 768E^3 - 92E^4}{288n^2} \right)$$

(3)

where n is the number of spikes, and $Z=n r^2$ (Fisher, 1993). Events were considered to be phase-coupled, if the Rayleigh test indicated that they were not distributed randomly around the ripple cycle ($p_r < 0.05$)(Zar, 1999). The circular standard deviation reported in Table 1 was taken as

$$\sigma = \sqrt{-2 \ln r} \quad (4)$$

where r is the phase-coupling strength (Zar, 1999).

To test equality of means of angular variables the multi-sample Watson-Williams test was used. Circular statistics were performed using Oriana 2.0 software (Kovach Computing Services, Anglesey, UK).

Results

In the CA3 region of mouse hippocampal slices, synchronous network events closely resembling SWRs recorded *in vivo* can be detected (Csicsvari et al., 2000; Maier et al., 2003). These synchronous activities occurred spontaneously at a rate of 1.1 ± 0.08 Hz ($n=92$ slices), and the frequency of the accompanying ripple oscillations was 185.8 ± 1.3 Hz ($n=92$)(Figure 1A-C). Current source density analysis of SWRs showed a characteristic laminar profile with a dominant source in the stratum pyramidale and a dominant sink in the proximal part of the stratum radiatum bordered by a weaker source in the distal part of the stratum radiatum (Figure 1D), comparable to that observed in intact animals or in other models of SWRs (Ellender et al., 2010; Sullivan et al., 2011). To characterize these events in more details, we measured the peak amplitude (144.3 ± 9.5 μ V; $n=92$) and the half width of sharp waves (17.8 ± 0.45 ms; $n=92$), as well as the number of ripple cycles/event (4.2 ± 0.2 ; $n=92$) and the area of ripple oscillations (0.17 ± 0.01 μ V, $n=92$) of those events that were recorded within the stratum pyramidale. When we compared the sharp wave amplitude with the area of ripple oscillations recorded in different slices, we found a significant correlation (Figure 1E), indicating that these two events may share a common origin and/or generating mechanisms. In contrast, there was no relationship between the sharp wave amplitude and their incidence compared among slices (Figure 1F).

Recorded neuron types in CA3

To uncover the spiking behavior and the synaptic input of distinct neuron types in CA3 during SWRs, we concomitantly recorded local field potentials together with action potentials in loose-patch mode and subsequently postsynaptic currents in whole-cell mode. The intracellularly labeled neurons were then anatomically identified. Based on the dendritic and axonal arborization, recorded neurons were grouped *post hoc* into nine anatomical types (Freund and Buzsáki, 1996; Somogyi and Klausberger, 2005) and their input-output properties in relation to the SWRs were compared. Pyramidal cells had spiny dendrites spanning all layers and their rarely branching axons were found mainly in the stratum oriens and partially in the stratum radiatum (PC, n=16, Figure 2A). Three interneuron types having axons prevalently in pyramidal cell layer were distinguished. In PV-EGFP mice, we sampled both basket cells (PV+BC, n=9) and axo-axonic cells (AAC, n=10). Their dendrites found in all layers were either smooth or occasionally decorated with some spines. Axon arbor of both cell types was predominantly present in the stratum pyramidale (Figure 2A). Another type of basket cells expressing cholecystokinin and CB1 cannabinoid receptors was recorded in slices prepared from GAD65-EGFP mice (CB1+BC, n=13). The majority of these interneurons had radial dendrites spanning all layers (n=11), while the dendritic tree of two basket cells was mostly restricted to the stratum oriens. The axon of all basket cells ramified mainly in the stratum pyramidale, but some axon collaterals could be observed both in the strata lucidum and oriens (Figure 2A).

Five interneuron types were separated with axons projecting to the dendritic layers; three of them had horizontal dendrites in the stratum oriens, while the dendritic tree of the remaining two cell types had spherical appearance. Dendrites of OLM cells bearing elongated filopodia-like spines were exclusively found in the stratum oriens, while their axons were present both in the strata oriens and lacunosum-moleculare. These interneurons were sampled either in slices prepared from the PV-EGFP mice (n=2), or from wild type mice (n=3)(OLM, n=5, Figure 2A). We also distinguished oriens-oriens cells, their smooth dendrites and often ramifying axons were restricted to the stratum oriens (OO, n=4, Figure 2A). The most abundant cell type in our sample was the oriens-radiatum cell (OR, n=16, Figure 2A). Their smooth or spiny dendrites were present in the stratum oriens, while their rarely ramifying axons could be observed typically in the strata oriens and radiatum, and occasionally penetrating into the CA1 region. These GABAergic neurons resemble those that project outside the hippocampus (Gulyas et al., 2003; Jinno et al., 2007). Radiatum cells (RAD, n=9) were sampled either in slices prepared from the GAD65-EGFP mice (n=5), or from wild type

mice (n=4)(Figure 2A). In both cases, the smooth dendrites of these interneurons as well as their axon arbor were found largely in the stratum radiatum and partially in stratum lucidum, rarely penetrating into the stratum oriens. The last distinguished neuron type was the ivy cell (n=5, Figure 5C). The somata and the extension of the dendritic tree of ivy cells were smaller than those observed for other neurons. Their cell bodies were found in the stratum pyramidale or in its close vicinity. Their smooth dendrites as well as their axons ramified extensively around the somata, forming a dense local meshwork, but these cells do not express either PV or cholecystokinin, a marker of CB1+BCs (Fuentelba et al., 2008). In this study, we have not recorded any bistratified cells in CA3, which interneuron type was described first in CA1 (Buhl et al., 1994).

Firing behavior of CA3 neurons during SWRs

Overall, we observed that only the minority of pyramidal cells fired during SWRs. From 59 pyramidal cells tested (16 was verified with biocytin labeling, while the others using DIC image), ten neurons, all labeled intracellularly, discharged single action potentials during ~ 6 % of these synchronous events on average. In contrast, the majority of interneurons (77 %; 55 from 71) emitted one or more spikes during SWRs. The firing activity of interneurons showed cell type-specific behavior. Between SWRs, interneurons were more active than pyramidal cells (M-W test, $p < 0.001$), while the firing rate of perisomatic region-targeting interneurons (PV+BC, AAC, CB1+BC) and dendritic layer-innervating interneurons (OLM, OO, OR, RAD) did not differ (M-W test, $p = 0.22$). During SWRs, pyramidal cells emitted the least number of spikes compared to all interneurons (Figure 2B, Table 1, t-test, $p < 0.001$). Similarly to the averaged spiking activity between SWRs, perisomatic region-targeting interneurons fired comparable number of spikes during SWRs than dendritic layer-innervating interneurons (Figure 2B, Table 1, t-test, $p = 0.44$). In the former cell groups, however, PV+BCs spiked more during SWRs than AACs and CB1+BCs (ANOVA, $p < 0.001$), while in the latter group the number of spikes did not differ in cell categories (ANOVA, $p = 0.62$)(Figure 2B, Table 1). The only interneuron type, which did not spike during SWRs, was the ivy cell (n=5). Among CB1+BCs and RAD cells we found a substantial number of cells being silent during SWRs.

We calculated the probability of firing for all cell types during SWRs. The active pyramidal cells fired single action potentials during smaller portion of these synchronous events than interneurons (M-W test, $p < 0.001$), but the perisomatic region-targeting interneurons and dendritic-layer-innervating interneurons did not differ in this respect (M-W

test, $p=0.54$). However, there was a significant difference in the proportion of SWRs with spikes between basket cells and AACs (ANOVA, $p=0.01$), but not between interneurons innervating the dendritic layers (ANOVA, $p=0.46$)(Figure 2C, Table 1). In the former cell class, PV+BCs fired on the larger portion of SWRs than AACs or CB1+BCs (Figure 2C, Table 1). We then analyzed the number of spikes during those SWRs when the cell fired. We found that pyramidal cells fired less action potentials compared to all interneurons (Figure 2D, Table 1, M-W test, $p<0.001$). In addition, the perisomatic region-targeting interneurons tended to fire more action potentials than dendritic-layer-innervating interneurons, although the difference did not reach significance (M-W test, $p=0.08$). Among perisomatic region-targeting interneurons, PV+BCs fired significantly more spikes during a SWR than AACs or CB1+BCs (ANOVA, $p<0.001$), while no difference was found in case of cell types innervating the dendritic layers (K-W ANOVA, $p=0.21$)(Figure 2D, Table 1). Next, we calculated the number of spikes during a ripple cycle by dividing the number of all spikes detected during ripple oscillations with the number of ripple cycles. We found no example for cells discharging more than a spike per a ripple cycle, therefore this value gives the probability of discharge during a ripple cycle. In this analysis only those cells were included, whose firing was significantly phase-coupled ($p_r<0.05$) to the ripple cycles determined with Rayleigh probability test. Similarly to what we found for SWRs, pyramidal cells were significantly less active during ripple oscillations than interneurons (M-W test, $p=0.014$). Furthermore, we found that the spike number during a ripple cycle was similar for interneurons innervating the perisomatic or dendritic layers of pyramidal cells, when comparing these two functionally distinct groups (M-W test, $p=0.36$). The comparison of the number of spikes during a ripple cycle within these two groups uncovered that PV+ BCs discharged more spikes than AACs (t-test, $p=0.005$), but cell types in the dendritic-layer-innervating group did not differ (K-W ANOVA, $p=0.88$)(Figure 2E, Table 1).

In the following sets of analysis we constructed the spike distribution histograms for each active neuron relative to the peak of the sharp wave envelop (zero point on the x axis). The histograms were skewed towards the left with different extent, indicating that neurons tend to fire before the peak of the SWRs. The asymmetry in spike distribution histograms differed between pyramidal cells and interneurons (M-W test, $p<0.001$), but not between perisomatic region-targeting interneurons and dendritic layer-innervating interneurons (M-W test, $p=0.72$). While there was no difference in the asymmetry in spike distribution histograms among dendritic layer-innervating interneurons (K-W ANOVA, $p=0.13$), basket cells and AACs differed in this respect (K-W ANOVA, $p=0.02$)(Figure 3A, Table 1). Namely, the

asymmetry was less pronounced for PV+BCs than for AACs ($p=0.004$, Table 1). Other comparisons showed no significant differences ($p=0.46$ for PV+BCs vs. CB1+BCs; $p=0.22$ for AACs vs. CB1+BCs; Table 1). When the zero point on the x axis of the histograms was set to the largest negative peak of the ripple oscillation, the plots showed more symmetric appearance in most cases, since the peak of ripple power always preceded the peak of SWRs by 1.43 ± 0.41 ms ($n=61$)(Figure 3B). We also calculated the phase and the coupling strength of the firing relative to the negative peak of ripple oscillation. Four of the ten pyramidal cells that fired had phase-coupled spikes ($p_r<0.05$). Among perisomatic region-targeting interneurons, all PV+BCs, all, but one AAC, and one of the CB1+BCs showed phase-coupled firing ($p_r<0.05$). The firing of OLM cells, OO cells and half of the OR cells were comparably coupled to the ripple oscillation, while RAD cells were weakly phase coupled (Figure 3B, C, $p_r<0.05$, Table 1). Circular statistical analysis revealed that the mean phase of spiking of all neurons was significantly different (Watson-Williams F-test for phase data, $p=0.013$, Table 1), namely, pyramidal cell fired at the distinct phase of ripple oscillations compared to all interneurons ($p<0.05$). In contrast, the coupling strength of spiking was similar in all cell types (ANOVA for vector data, $p=0.14$, Figure 3C, Table 1). In addition, we also calculated the spike time of spikes relative to the negative peak of ripple oscillation and found, in line with above data, that spike times were different (Table 1, ANOVA, $p=0.01$). Again, pyramidal cells fired earlier compared to the firing of the other cell types ($p<0.05$).

These data show that in slices only a small fraction of excitatory pyramidal cells is active during SWRs, rarely emitting single action potentials, which occur at different phase of ripple oscillations than the spikes in interneurons. In contrast, interneurons usually spike during every SWR. Among all interneurons, PV+BCs fired the most action potentials, while other GABAergic cells discharged similar number of spikes during SWRs.

Synaptic currents in CA3 neurons during SWRs

Following the detection of spikes in loose-patch mode, we recorded synaptic currents from the same neurons in whole-cell patch-clamp mode with a different pipette (Figure 4; see Methods). EPSCs were recorded at the reversal potential of IPSCs, (between - 85 and -75 mV) determined experimentally for each neuron, while IPSCs were measured close to the reversal potential of EPSCs (between 0 and + 20 mV). To be able to compare the synaptic inputs for individual cells recorded at different holding potentials, we calculated the synaptic conductance (see Methods) and used these values in the further analysis. First we analyzed the

recordings only for those neurons that spiked during SWRs. In this dataset, we observed that the synaptic excitation recorded in pyramidal cells was smaller than those measured in interneurons (Figure 4B, Table 2, M-W test, $p=0.003$), whereas the magnitude of excitatory postsynaptic conductance (EPSC) was similar in perisomatic region-targeting interneurons and dendritic layer-innervating inhibitory cells (Figure 4B, Table 2, M-W test, $p=0.14$). A more detailed analysis revealed that the synaptic excitation received by distinct types of perisomatic region-targeting interneurons was different (K-W ANOVA, $p=0.01$). EPSCs recorded in CB1+ BCs during SWRs were smaller in magnitude than in PV+ BCs ($p=0.008$), while other comparisons between those cell groups targeting the perisomatic region of pyramidal cells uncovered no difference ($p>0.3$). In dendritic layer-innervating interneurons the magnitude of EPSC was found not to be distinct using K-W ANOVA test ($p=0.066$). In contrast to synaptic excitation, the synaptic inhibition measured during SWRs was similar in pyramidal cells and interneurons (Figure 4C, Table 2, M-W test, $p=0.69$), and the magnitude of inhibitory postsynaptic conductance (IPSC) during SWRs received by perisomatic region-targeting interneurons was comparable to that recorded in dendritic layer-innervating interneurons (M-W test, $p=0.065$), as well as within these broad cell categories the synaptic inhibition was similar (K-W ANOVA, $p=0.07$ for perisomatic region-targeting interneurons and $p=0.13$ for dendritic layer-innervating interneurons). The ratio of excitation to inhibition in pyramidal cells was below one (Figure 4D, Table 2), indicating that the inhibitory synaptic input is dominant in these neurons during SWRs. The ratio of EPSC and IPSC in interneurons was around one or was larger, suggesting that synaptic excitation is prevailing in GABAergic cells during SWRs (Figure 4D, Table 2). EPSC/IPSC ratio obtained in pyramidal cells was significantly smaller than those calculated for interneurons (M-W test, $p<0.001$), whereas among interneurons there was no significant difference in this ratio (M-W test, $p=0.69$ for the comparison between perisomatic region-targeting interneurons and dendritic layer-innervating interneurons; K-W ANOVA, $p=0.16$ and $p=0.82$ for the group of perisomatic region-targeting interneurons and dendritic layer-innervating interneurons, respectively).

Next, we calculated the synaptic inputs in neurons, which were silent during SWRs, and the results were compared to those cells that were active (Figure 5, Table 2). Such analysis could be made for pyramidal cells, CB1+BCs and RAD cells. We found that the synaptic excitation was similar in active and silent pyramidal cells (t-test, $p=0.82$), but it was significantly larger in spiking interneurons compared to their silent pairs (t-test, $p=0.005$ for CB1+ BCs; M-W test, $p=0.03$ for RAD cells). On the contrary, significantly smaller inhibition was received by those pyramidal cells that spiked during SWRs than the silent ones

(t-test, $p=0.02$), whereas IPSP in the active and silent interneurons was comparable (t-test, $p=0.92$ for CB1+ BCs; $p=0.29$ for RAD cells). Therefore, the ratio of EPSP/IPSP in spiking cells in each cell type was larger than in silent cells (t-test, $p=0.02$ for pyramidal cells; t-test, $p=0.008$ for CB1+ BCs; M-W test, $p=0.048$ for RAD cells). Thus, smaller synaptic inhibition resulted in larger EPSP/IPSP ratio in spiking pyramidal cells compared to silent ones, while larger synaptic excitation was detected in spiking interneurons than in their silent pairs during SWRs.

We also examined the synaptic inputs of ivy cells during SWRs. These interneurons, which were uniformly silent during SWRs, received smaller synaptic excitation (EPSP: 18.6 ± 11.8 , $n=4$) than inhibition (IPSP: 28.7 ± 15.9 , $n=4$), as reflected in their EPSP/IPSP ratio (E/IPSP: 0.66 ± 0.12 , $n=4$)(Figure 5).

To gain deeper insights into the link between the synaptic inputs and the firing output of neurons during SWRs, we related the synaptic conductance with the number of spikes. Since the above data propose that the firing of pyramidal cells and interneurons during SWRs might be distinctly controlled by excitatory and inhibitory synaptic inputs, we investigated the input-output relationship separately. In pyramidal cells, we found a no tendency between the EPSP and the number of spikes, between IPSP and the number of spikes, or between the EPSP/IPSP ratio and the number of spikes during SWRs (Figure 6A, C, E). In contrast, there was a strong correspondence between the magnitude of EPSP and the number of spikes in interneurons during these synchronous network events (Figure 6B). Even though, no link was observed between the magnitude of IPSP and the number of spikes in interneurons (Figure 6D), their EPSP/IPSP ratio still correlated with the number of spikes during SWRs (Figure 6F).

In summary, in pyramidal cells the recorded inhibitory synaptic input dominates over the synaptic excitation during SWRs, while, in case of interneurons it is quite the opposite, excitatory synaptic input is larger than synaptic inhibition. The comparison of the inputs in active and silent cells during SWRs as well as the relationship between the magnitude of the synaptic inputs and spike number suggests that pyramidal cell firing **can be** controlled by synaptic inhibition fluctuating between SWRs, whereas the magnitude of the excitatory synaptic input regulates the spiking activity of interneurons.

Comparison of the firing histograms and the temporal structure of synaptic inputs during SWRs

Next, we asked whether the observed asymmetry in spike distribution histogram relative to the sharp wave peak envelop could be the result of the asymmetry in excitatory synaptic input, since excitation is a main determinant of spiking, at least in interneurons. To clarify this issue, we calculated the magnitude of EPSG and IPSG as well as their ratios for the period before the peak (Pre SWR peak) and after the peak (Post SWR peak) of sharp wave envelop (Figure 7A). A weak, but significant correlation was observed in the asymmetry of spike distribution histogram with the ratio of EPSG before and after the peak of sharp wave envelops (Figure 7B). No other comparison of the histogram asymmetry with additional parameters of synaptic inputs showed any significant link. These results propose that asymmetry in spiking during SWRs may be, at least in part, the consequence of the asymmetry in the excitatory synaptic input.

This detailed analysis also uncovered some additional interesting results. We observed substantial cell-type specific differences in inputs of those interneurons that have comparable soma-dendritic appearance in CA3 network and thus are expected to collect the same inputs. When we compared the temporal structure of SWR-related synaptic inputs of pyramidal cells and perisomatic region-targeting interneurons located close to the stratum pyramidale, which neurons have almost exclusively radial dendritic arbor spanning all layers and might receive synaptic inputs from the same sources during SWRs, we found that the magnitude of EPSG before the peak and after the peak of SWR was significantly different (ANOVA, $p < 0.001$ and $p = 0.004$, for Pre Peak EPSG and Post Peak EPSG, respectively; Figure 7C, D, Table 3). The Fisher post hoc test confirmed that before the peak of SWRs PV+BCs received significantly larger synaptic excitation than pyramidal cells, AACs or CB1+BCs, a difference, which was similar also after the peak of SWRs (Figure 7C, D, Table 3). EPSGs before, but not after, the peak of SWRs was larger in AACs than in pyramidal cells or CB1+BCs (Figure 7C, D, Table 3). Consequently, the ratio of Pre/Post SWR peak EPSG was larger for AACs, than for pyramidal cells, PV+BCs or CB1+BCs on average (ANOVA, $p = 0.001$, Figure 7G, Table 3), indicating that in AACs the magnitude of the excitatory input is smaller after the peak of SWRs than before, which was opposite to that observed in pyramidal cells or basket cells. In addition to the excitatory input, there were some significant differences also in the temporal structure of synaptic inhibition after the peak of SWRs (Post Peak IPSG, ANOVA, $p = 0.004$), but not before it (Pre Peak IPSG, ANOVA, $p = 0.07$) (Figure 7E, F). Namely, pyramidal cells and AACs received comparable IPSGs after the peak of SWRs, and, similarly, the two types of basket cells collected equal synaptic inhibition (Figure 7F, Table 3). Moreover, after the SWR peak IPSGs in AACs were significantly larger than in the basket cells and IPSGs in

pyramidal cells were larger than in CB1+BCs (Figure 7F, Table 3). However, the ratio of Pre/Post SWR peak IPSPG was not different (ANOVA, $p=0.41$; Figure 7H, Table 3). When the ratio of EPSPG/IPSPG before the peak of SWRs was compared with the ratio of EPSPG/IPSPG after the peak, we found that PV+BCs received larger excitation than inhibition before as well as after the SWR peak than pyramidal cells or other types of perisomatic region-targeting interneurons (ANOVA, $p<0.001$ and $p=0.002$ for Pre Peak E/IPSPG and Post Peak E/IPSPG, respectively; Figure 7I, J, Table 3). While the temporal structure of synaptic input did not change in pyramidal cells or in basket cell (Figure 7I, J), EPSPG before the SWR peak in AACs was larger than IPSPG, which was reversed after the SWR peak (t-test, $p=0.004$).

In addition to perisomatic region-targeting interneurons, we also compared the fine structure of synaptic inputs during SWRs in interneurons with horizontal dendrites in the stratum oriens, since they might be innervated by the same afferents. Indeed, we found that in general these cells had comparable synaptic inputs before and after the SWR peak ($p>0.1$) with two exceptions. OLM cells received a slightly larger EPSPG after the SWR peak than OR cells ($p=0.02$), and IPSPG was larger before the SWR peak in OO cells than in OR cells ($p=0.01$, Table 3).

This detailed examination of synaptic inputs during SWRs suggest that, while dendritic layer-innervating interneurons located in the stratum oriens receive comparable synaptic inputs during SWRs, in distinct types of GABAergic cells innervating the perisomatic region of pyramidal cells we measured significantly different synaptic excitation and/or inhibition during these population events, which might, at least in part, explain some of the differences in their spiking behavior.

Interaction between excitatory and inhibitory synaptic conductances during SWRs

In the last set of the analysis, we determined the combined effect of synaptic inputs during SWRs (Borg-Graham et al., 1998; de la Prida and Gal, 2004; Oren et al., 2006). To reveal the interaction between inhibitory and excitatory synaptic conductances, we calculated the net apparent synaptic reversal potential E_{syn}^{app} (see Methods). E_{syn}^{app} describes the effective synaptic conductance during these synchronous events, and thus, provides a measure of the balance of excitation and inhibition. We observed that the maximums and the minimums of the spike distribution histograms were tightly coupled to the peaks and the troughs in the 'ripple'-like appearance of E_{syn}^{app} , respectively, indicating that the excitatory and inhibitory

synaptic conductances shape together the firing of interneurons during SWRs (Figure 8A, B). In addition, we found that the averaged E_{syn}^{EPSP} curves showed cell-type dependence both in their peak values and their appearance (Figure 8C). In those cell groups, in which the peak of E_{syn}^{EPSP} approached closer the reversal potential of the synaptic excitation, more spikes could be detected (Figure 8D), confirming that the magnitude of excitatory synaptic input controls the spiking activity during SWRs, at least in interneurons. Moreover, the asymmetry in the spike distribution histograms relative to the sharp wave peak matched the asymmetry in E_{syn}^{EPSP} as shown in examples in Figure 8A, B. At population levels, in PV+BCs and OLM cells, in which interneuron types the asymmetry index of spike distribution histograms was close to 1 (Table 1), the appearance of the averaged E_{syn}^{EPSP} curves was also more symmetric, while in other cell types the E_{syn}^{EPSP} reached its maximum before or around the peak of the sharp waves, followed by the abrupt drop toward more negative values (Figure 8C). We calculated the asymmetry index of E_{syn}^{EPSP} in individual cells, similarly to the asymmetry index of spike distribution histograms (Figure 7A). While no relationship was observed between the asymmetry index of E_{syn}^{EPSP} and the asymmetry index of spike distribution histograms in pyramidal cells (Figure 8E), there was a strong correlation between these values in interneurons (Figure 8F).

These results strengthen the idea that in interneurons the number of discharges during SWRs is primarily determined by the magnitude of synaptic excitation, and suggest that the spike distribution during these network events is shaped by the temporal dynamics of both excitatory and inhibitory synaptic inputs. The firing of pyramidal cells during SWRs, however, is controlled mainly by other factors.

Discussion

As *in vivo* studies uncovered, SWRs are generated in the CA3 region of the hippocampus (Csicsvari et al., 2000; Maier et al., 2003; Nakashiba et al., 2009). Within the same hippocampal area, population events with similar appearance can be recorded in rodent slices, where they occur spontaneously and when the content of aCSF is modified,

respectively, or they are evoked by electrical stimulation (Kubota et al., 2003; Maier et al., 2003; Behrens et al., 2005; Wu et al., 2005; de la Prida et al., 2006; Ellender et al., 2010). Although these synchronous population events in slices are shorter in duration than those recorded *in vivo*, the *in vitro* SWRs share several features with their *in vivo* equivalents, including the emergence of a large deflection in local field potential concomitant with high frequency oscillation, the characteristic increase in firing rate of neurons during SWRs and the typical laminar profile of current sinks and sources during these events. These striking similarities in synchronous population events observed in slices with those recorded *in vivo* propose that the *in vitro* approach might serve as a model for *in vivo* SWRs, grabbing some of their key features.

In this study we found that only a small portion of pyramidal cells became active during SWRs and pyramidal cells discharge at the different phases of the CA3 ripple oscillation than interneurons (Figure 3), similar to *in vivo* results (Csicsvari et al., 2000; Sullivan et al., 2011). The low number of active pyramidal cells during SWRs in slices may be due to the smaller size of the neuronal ensemble generating these *in vitro* synchronous events compared to *in vivo* and/or the lack of extrahippocampal inputs, which could impact the amount of pyramidal cells recruited into these network activities. The firing activity of anatomically-identified interneurons during *in vivo* SWRs is already known for CB1+ basket and dendritic layer-innervating cells from CA3 (Lasztoczi et al., 2011). Similarly to the data obtained in anesthetized rats, we observed in slices that CB1+BCs were only weakly recruited during SWRs, since only a part of these interneurons were found to spike, and if they spiked, single action potentials were detected at every third events on average. Comparable firing behavior was observed for dendritic layer-innervating cells. In addition, the firing behavior of distinct types of CA1 interneurons during SWRs is impressively similar to that we obtained in CA3 hippocampal slices. For instance, PV+BCs are one of the most active interneuron types, while ivy cells were found to be silent (Fuentelba et al., 2008; Lapray et al., 2012; Varga et al., 2012). Furthermore, OLM cells increase their firing under these population events in freely moving animals (Varga et al., 2012). The comparable spiking behavior of the anatomically-identified neurons during SWRs *in vitro* and *in vivo* further strengthen the idea that the *in vitro* model can be used to reveal the synaptic mechanisms underlying the firing properties of distinct types of neurons.

Synaptic inputs distinctly influences the firing of pyramidal cells and interneurons during SWRs

One of our main observations in this study is that the synaptic inhibition is dominant in pyramidal cells during SWRs, while excitation dominates the synaptic inputs of active interneurons. While the magnitude of recorded excitatory input in active and silent pyramidal cells was comparable, in the former group smaller inhibitory synaptic charge was measured than in the latter, indicating that synaptic inhibition plays a role in controlling the spiking of pyramidal cells during *in vitro* SWRs. In contrast, larger synaptic excitation was present in active interneurons than in non-spiking cells within the same anatomical categories. Moreover, there was a strong correlation between the magnitude of excitatory synaptic charge and the number of spikes during SWRs including all spiking interneurons (Figure 6B, 8D). These data are reminiscent of those found in a previous study investigating the input-output properties of distinct classes of CA3 neurons during gamma oscillation *in vitro* (Oren et al., 2006). The strikingly similar observations in the synaptic mechanisms governing the firing behavior of excitatory and GABAergic neurons during gamma oscillations and SWRs propose that neurons are integrating similarly their synaptic inputs during these network states. However, it should be noted that besides the synaptic inputs the firing of distinct neuron types during SWRs could be also affected by single-cell properties, including the firing thresholds or passive and active membrane features, or other factors.

Distinct types of interneurons receive different synaptic inputs during SWRs

The analysis of the temporal structure of synaptic inputs in relation to the SWR peak uncovered that the magnitudes of excitatory and inhibitory synaptic charge as well as their ratios were very different in the three types of interneurons innervating the perisomatic region of pyramidal cells. This finding corresponds to the anatomical observations that PV+ interneurons receive three times more excitatory, but the same number of inhibitory synapses, than CB1+BCs (Gulyas et al., 1999; Matyas et al., 2004). These data and the observation that fast spiking (i.e. PV+) interneurons could be excited more easily by intrahippocampal afferents than regular spiking (i.e. CB1+) basket cells (Glickfeld and Scanziani, 2006) are in line with our results showing that PV+BCs received larger synaptic excitation, but similar synaptic inhibition during SWRs than CB1+BCs. The former cells also discharged more spikes than the latter interneurons. Neither previous anatomical works nor electrophysiological studies have compared the input properties of PV+BCs and AACs to each other in the hippocampus. Our present data propose that either their dendritic arborization pattern or the synaptic features of their afferents should be significantly different. First, much larger synaptic inhibition was recorded during SWRs in AACs than in PV+BCs,

implying that AACs receive more numerous and/or stronger inhibitory synaptic inputs from PV+BCs than PV+BCs from each other, if the main source of perisomatic inhibition during SWRs is originated from PV+BCs. Second, we observed a change in the temporal structure of synaptic inputs received by AACs during SWRs relative to the sharp wave peak, which was not detected in PV+ or CB1+BCs. This change in synaptic charge recorded in AACs during SWRs may reflect an enhanced synaptic inhibition after the sharp wave peak relative to the IPSP before the peak (Figure 7H, 8B, C), and/or a reduced synaptic excitation after the sharp wave peak relative to the EPSP before the peak (Figure 7G). The latter scenario is unlikely, since no evidence implies so far that PV+BCs and AACs receive excitatory inputs from distinct sets of CA3pyramidal cells, which could explain our findings. In any case, AACs should receive different inputs than basket cells and/or the short-term dynamics of these afferents could be dissimilar. Indeed, data from other cortical regions argue for the difference in synaptic inputs. For instance, AACs were found to be excited differently than basket cells by sensory input in the neocortex (Zhu et al., 2004) or upon noxious stimulus in the basolateral amygdala (Bienvenu et al., 2012), suggesting distinct excitatory recruitment of AACs in cortical networks.

The number of excitatory input onto GABAergic projection neurons (resembling OR cells in this study) was found to be comparable to PV+ interneurons (Gulyas et al., 1999; Takacs et al., 2008). While both of these cell types significantly increase their firing rate to a similar extent during SWRs *in vivo* (Klausberger et al., 2003; Jinno et al., 2007; Lapray et al., 2012; Varga et al., 2012), OR cells spiked less and received smaller EPSPs than PV+BCs during SWRs in hippocampal slices. This contradiction might imply that PV+BCs may receive a larger number of excitatory inputs from surrounding pyramidal cells, thus, are entrained by the activity of local neuronal networks (which is more intact in slices), whereas GABAergic projection cells could monitor more global changes in hippocampal activity.

Perisomatic inhibition is one of the main sources of the field signal of SWRs in the stratum pyramidale

Our results propose that in CA3 the synaptic output of GABAergic cells substantially contributes to the deflection in LFP, which might be reflected as an active source during SWRs (Figure 1D). In accord, blocking of GABA_A receptor-mediated synaptic transmission eliminates SWRs in CA3 *in vitro* (Maier et al., 2003; Ellender et al., 2010). The large current source restricted to the stratum pyramidale suggests that perisomatic region-targeting interneurons are the most likely candidates playing key roles in SWR generation *in vitro*.

Since AACs and CB1+BCs are much less active interneurons during SWRs than PV+BCs, we propose that the recruitment of these latter perisomatic region-targeting interneurons by local pyramidal cell ensembles is the crucial step in SWR generation.

In CA3, both gamma oscillations and SWRs are generated during different behavioral states in freely moving animals (Chrobak et al., 2000). Strikingly, these mutually exclusive oscillations, accompanying distinct neuronal information processing modes (Buzsáki, 2006), might be produced by the same neuronal circuit composed of recurrently connected pyramidal cells and PV+BCs in the CA3 region of the hippocampus (Gulyas et al., 2010). An exciting question for future research is related to the switch between information processing modes in SWR- and gamma oscillation-related network operations within the same rhythm-generating network.

Reference list

- Atallah BV, Scanziani M (2009) Instantaneous modulation of gamma oscillation frequency by balancing excitation with inhibition. *Neuron* 62:566-577.
- Behrens CJ, van den Boom LP, de Hoz L, Friedman A, Heinemann U (2005) Induction of sharp wave-ripple complexes in vitro and reorganization of hippocampal networks. *Nat Neurosci* 8:1560-1567.
- Bienvenu TC, Busti D, Magill PJ, Ferraguti F, Capogna M (2012) Cell-type-specific recruitment of amygdala interneurons to hippocampal theta rhythm and noxious stimuli in vivo. *Neuron* 74:1059-1074.
- Borg-Graham LJ, Monier C, Fregnac Y (1998) Visual input evokes transient and strong shunting inhibition in visual cortical neurons. *Nature* 393:369-373.
- Buhl EH, Halasy K, Somogyi P (1994) Diverse sources of hippocampal unitary inhibitory postsynaptic potentials and the number of synaptic release sites *Nature* 368:823-828.
- Buzsáki G (1986) Hippocampal sharp waves: their origin and significance. *Brain Res.* 398:242-252.
- Buzsáki G (1989) Two-stage model of memory trace formation: A role for 'noisy' brain states. *Neuroscience* 310:551-570.
- Buzsáki G (2006) *Rhythms of the brain*. Oxford University Press.
- Chrobak JJ, Buzsáki G (1996) High-frequency oscillations in the output networks of the hippocampal-entorhinal axis of the freely behaving rat. *J Neurosci* 16:3056-3066.
- Chrobak JJ, Lorincz A, Buzsaki G (2000) Physiological patterns in the hippocampo-entorhinal cortex system. *Hippocampus* 10:457-465.
- Csicsvari J, Hirase H, Mamiya A, Buzsaki G (2000) Ensemble patterns of hippocampal CA3-CA1 neurons during sharp wave-associated population events. *Neuron* 28:585-594.
- de la Prida M, Gal B (2004) Synaptic contributions to focal and widespread spatiotemporal dynamics in the isolated rat subiculum in vitro. *The Journal of neuroscience* 24:5525-5536.
- de la Prida LM, Huberfeld G, Cohen I, Miles R (2006) Threshold behavior in the initiation of hippocampal population bursts. *Neuron* 49:131-142.
- Dragoi G, Carpi D, Recce M, Csicsvari J, Buzsaki G (1999) Interactions between hippocampus and medial septum during sharp waves and theta oscillation in the behaving rat. *The Journal of neuroscience* : 19:6191-6199.

- Ellender TJ, Nissen W, Colgin LL, Mann EO, Paulsen O (2010) Priming of hippocampal population bursts by individual perisomatic-targeting interneurons. *The Journal of neuroscience* 30:5979-5991.
- Freund TF, Buzsáki G (1996) Interneurons of the hippocampus. *Hippocampus* 6:345 - 470.
- Fuentealba P, Begum R, Capogna M, Jinno S, Marton LF, Csicsvari J, Thomson A, Somogyi P, Klausberger T (2008) Ivy cells: a population of nitric-oxide-producing, slow-spiking GABAergic neurons and their involvement in hippocampal network activity. *Neuron* 57:917-929.
- Girardeau G, Benchenane K, Wiener SI, Buzsáki G, Zugaro MB (2009) Selective suppression of hippocampal ripples impairs spatial memory. *Nat Neurosci* 12:1222-1223.
- Glickfeld LL, Scanziani M (2006) Distinct timing in the activity of cannabinoid-sensitive and cannabinoid-insensitive basket cells. *Nat Neurosci* 9:807-815.
- Gulyas AI, Hajos N, Katona I, Freund TF (2003) Interneurons are the local targets of hippocampal inhibitory cells which project to the medial septum. *The European journal of neuroscience* 17:1861-1872.
- Gulyas AI, Megias M, Emri Z, Freund TF (1999) Total number and ratio of excitatory and inhibitory synapses converging onto single interneurons of different types in the CA1 area of the rat hippocampus. *The Journal of neuroscience* 19:10082-10097.
- Gulyas AI, Szabo GG, Ulbert I, Holderith N, Monyer H, Erdelyi F, Szabo G, Freund TF, Hajos N (2010) Parvalbumin-containing fast-spiking basket cells generate the field potential oscillations induced by cholinergic receptor activation in the hippocampus. *The Journal of neuroscience* 30:15134-15145.
- Hajos N, Ellender TJ, Zemankovics R, Mann EO, Exley R, Cragg SJ, Freund TF, Paulsen O (2009) Maintaining network activity in submerged hippocampal slices: importance of oxygen supply. *The European journal of neuroscience* 29:319-327.
- Jadhav SP, Kemere C, German PW, Frank LM (2012) Awake Hippocampal Sharp-Wave Ripples Support Spatial Memory. *Science* 336:1454-1458.
- Jinno S, Klausberger T, Marton LF, Dalezios Y, Roberts JD, Fuentealba P, Bushong EA, Henze D, Buzsáki G, Somogyi P (2007) Neuronal diversity in GABAergic long-range projections from the hippocampus. *The Journal of neuroscience* 27:8790-8804.
- Klausberger T, Magill PJ, Marton LF, Roberts JD, Cobden PM, Buzsáki G, Somogyi P (2003) Brain-state- and cell-type-specific firing of hippocampal interneurons in vivo. *Nature* 421:844-848.
- Klausberger T, Somogyi P (2008) Neuronal diversity and temporal dynamics: the unity of hippocampal circuit operations. *Science* 321:53-57.
- Kubota D, Colgin LL, Casale M, Brucher FA, Lynch G (2003) Endogenous waves in hippocampal slices. *Journal of neurophysiology* 89:81-89.

- Lapray D, Lasztoczi B, Lagler M, Viney TJ, Katona L, Valenti O, Hartwich K, Borhegyi Z, Somogyi P, Klausberger T (2012) Behavior-dependent specialization of identified hippocampal interneurons. *Nat Neurosci* 15:1265-1271.
- Lasztoczi B, Tukker JJ, Somogyi P, Klausberger T (2011) Terminal field and firing selectivity of cholecystinin-expressing interneurons in the hippocampal CA3 area. *The Journal of neuroscience* 31:18073-18093.
- Le Van Quyen M, Bragin A, Staba R, Crepon B, Wilson CL, Engel J, Jr. (2008) Cell type-specific firing during ripple oscillations in the hippocampal formation of humans. *The Journal of neuroscience* 28:6104-6110.
- Logothetis NK, Eschenko O, Murayama Y, Augath M, Steudel T, Evrard HC, Besserev M, Oeltermann A (2012) *Nature* 491:547-553.
- Lopez-Bendito G, Sturgess K, Erdelyi F, Szabo G, Molnar Z, Paulsen O (2004) Preferential origin and layer destination of GAD65-GFP cortical interneurons. *Cereb Cortex* 14:1122-1133.
- Maier N, Nimmrich V, Draguhn A (2003) Cellular and network mechanisms underlying spontaneous sharp wave-ripple complexes in mouse hippocampal slices. *J Physiol* 550:873-887.
- Matyas F, Freund TF, Gulyas AI (2004) Convergence of excitatory and inhibitory inputs onto CCK-containing basket cells in the CA1 area of the rat hippocampus. *The European journal of neuroscience* 19:1243-1256.
- Meyer AH, Katona I, Bлатow M, Rozov A, Monyer H (2002) In vivo labeling of parvalbumin-positive interneurons and analysis of electrical coupling in identified neurons. *The Journal of neuroscience* 22:7055-7064.
- Nakashiba T, Buhl DL, McHugh TJ, Tonegawa S (2009) Hippocampal CA3 output is crucial for ripple-associated reactivation and consolidation of memory. *Neuron* 62:781-787.
- Oren I, Hajos N, Paulsen O (2010) Identification of the current generator underlying cholinergically induced gamma frequency field potential oscillations in the hippocampal CA3 region. *J Physiol* 588:785-797.
- Oren I, Mann EO, Paulsen O, Hajos N (2006) Synaptic currents in anatomically identified CA3 neurons during hippocampal gamma oscillations in vitro. *The Journal of neuroscience* 26:9923-9934.
- Somogyi P, Klausberger T (2005) Defined types of cortical interneurone structure space and spike timing in the hippocampus. *J Physiol* 562:9-26.
- Sullivan D, Csicsvari J, Mizuseki K, Montgomery S, Diba K, Buzsaki G (2011) Relationships between hippocampal sharp waves, ripples, and fast gamma oscillation: influence of dentate and entorhinal cortical activity. *The Journal of neuroscience* 31:8605-8616.

- Takacs VT, Freund TF, Gulyas AI (2008) Types and synaptic connections of hippocampal inhibitory neurons reciprocally connected with the medial septum. *The European journal of neuroscience* 28:148-164.
- Ulbert I, Halgren E, Heit G, Karmos G (2001) Multi microelectrode-recording system for human intracortical applications. *J Neurosci Methods* 106:69-79.
- Varga C, Golshani P, Soltesz I (2012) Frequency-invariant temporal ordering of interneuronal discharges during hippocampal oscillations in awake mice. *Proc Natl Acad Sci U S A* 109:E2726-2734.
- Wu C, Asl MN, Gillis J, Skinner FK, Zhang L (2005) An in vitro model of hippocampal sharp waves: regional initiation and intracellular correlates. *Journal of neurophysiology* 94:741-753.
- Zar JH (ed) (1999) *Biostatistical analysis*. Upper Saddle River, NJ:Prentice Hall.
- Zhu Y, Stornetta RL, Zhu JJ (2004) Chandelier cells control excessive cortical excitation: characteristics of whisker-evoked synaptic responses of layer 2/3 nonpyramidal and pyramidal neurons. *The Journal of neuroscience* 24:5101-5108.

Figure legends

Figure 1. Sharp waves and associated ripple oscillations (SWRs) in hippocampal slices. A, In local field potential (LFP) recorded from the stratum pyramidale of the CA3 region, spontaneously occurring SWRs could be observed. Ripple band-pass filtered version of the same trace is shown below. B, Magnification of boxed SWR in A. C, Power spectral density function of the trace in A showing ripple frequency peak (arrow). D, LFP recorded with a laminar multielectrode array was used for calculating the current source density plot (below). A large sink (blue) and source (red) pair is present in the strata radiatum and pyramidale, respectively. The figure shows an individual LFP signal and a CSD obtained from this example signal. E, Correlation between the sharp wave amplitude and ripple area. F, The rate of SWRs was independent of sharp wave amplitude. Each point on these plots is an averaged value from individual experiments (n=79).

Figure 2. Firing properties of anatomically-identified neurons in CA3 during SWRs. A, Camera lucida reconstructions of intracellularly labeled neurons from each group are presented (dendrites, black; axon, red). Scale bars, 100 μ m. Spiking of individual neurons detected in loose patch mode was concomitantly recorded with SWRs. The firing activity of neurons during 15 consecutive SWRs are shown below the averaged SWRs (calculated from 50 events) for each case. Individual spikes are the positive deflections on the traces. Scale bar, 50 μ V. B, Pyramidal cells (PC) discharged the lowest number of spikes during SWRs than interneurons (a, $p<0.001$); perisomatic region-targeting interneurons and dendritic layer-innervating interneurons emitted similar number of spikes on average ($p=0.44$); PV+BCs spiked more than AACs and CB1+BCs (b, $p<0.001$ for PV+BC vs. CB1+BC, c, $p=0.005$ for PV+BC vs. AACs; $p=0.14$ for AAC vs. CB1+BC); no difference was found in cell types innervating the dendritic layers ($p=0.62$). C, While perisomatic region-targeting interneurons and dendritic layer-innervating interneurons fired similarly during almost all SWRs ($p=0.54$), PCs only spiked during smaller proportion, $\sim 6\%$ of these synchronous events on average (a, $p<0.001$). Again, perisomatic region-targeting interneurons and dendritic layer-innervating interneurons emitted similar number of spikes on average ($p=0.54$); PV+BCs spiked more than AACs and CB1+BCs (b, $p=0.003$ for PV+BC vs. CB1+BC, c, $p=0.04$ for PV+BC vs. AACs; $p=0.19$ for AAC vs. CB1+BC); no difference was found in cell types innervating the dendritic layers ($p=0.46$). D, Compared to all interneurons, pyramidal cells fired less action

potentials during those SWRs, when the cell fired (a, $p < 0.001$), while in perisomatic region-targeting interneurons and dendritic layer-innervating interneurons number of spikes emitted did not differ ($p = 0.082$). Among perisomatic region-targeting interneurons, PV+BCs spiked more than AACs and CB1+BCs (b, $p < 0.001$ for PV+BC vs. CB1+BC, $p = 0.008$ for PV+BC vs. AACs; $p = 0.12$ for AAC vs. CB1+BC), while no difference was found in cell types innervating the dendritic layers ($p = 0.21$). E, Pyramidal cells emitted significantly less spikes during ripple cycles than interneurons (a, $p = 0.014$), while perisomatic region-targeting interneurons and dendritic layer-innervating interneurons discharged similar number of spikes ($p = 0.36$). In addition, PV+ BCs discharged more spike during a ripple cycle than AACs (b, $p = 0.005$), but cell types in the dendritic layer-innervating group discharged similar number of action potentials. In this graph only those neurons were included where the phase-coupling was significant (Rayleigh probability test; $p_r < 0.05$). Here on the box charts and in Figure 4, 5, 7, the mean (small open square), the median (midline of the big box), the interquartile range (large box), the 5/95% values (end of the whiskers), and the minimal/maximal values (bottom and top X symbols) are shown. Asterisk labels the significant differences. See Table 1 for details.

Figure 3. Spike distribution histograms of CA3 neurons during SWRs. A, Spike distribution histograms shown for individual neurons (gray) and their average (red) relative to the peak of the SWR envelop. In some neuron types, the asymmetry of the spike histograms relative to the SWR envelop peak is pronounced. Numbers in the upper right indicate the number of neurons that discharged during SWRs from all recorded and anatomically-identified neurons. B, Spike distribution histograms for each neuron (gray) and their average (red) relative to the peak of the largest negative ripple cycle. Numbers in the upper right indicate the number of neurons whose spiking was phase-coupled to ripple oscillation (Rayleigh probability test; $p_r < 0.05$). C, Polar plots indicate the phase and the strength of the ripple phase-coupled (black circle) and non-phase coupled (open circle) individual neurons. Red circle indicates the mean phase and strength calculated only from data of phase-coupled cells. See Table 1 for details.

Figure 4. Synaptic excitation and inhibition during SWRs. A, For each cell type, averaged SWRs, EPSCs recorded at holding potentials between -70 and -80 mV and IPSCs at 0 and +20 mV are shown. These traces were calculated from the averaged traces obtained in all neurons that spiked during SWRs (EPSC, red; IPSC, blue). Scale bars, 50 μ V for SWRs; 100 pA and 25 ms for PSCs. B, EPSG recorded during SWRs was significantly smaller in

pyramidal cells than in interneurons (a, $p=0.003$), whereas EPSG was similar in perisomatic region-targeting interneurons and dendritic layer-innervating inhibitory cells ($p=0.14$). Furthermore, EPSGs recorded in CB1+BCs were smaller in magnitude than in PV+ BCs (b, $p=0.008$), while other comparisons did not reveal any differences between perisomatic region-targeting interneurons ($p>0.3$), or between those cell groups targeting the dendritic region of pyramidal cells ($p=0.066$). C, IPSP during SWRs was similar in pyramidal cells and interneurons. D, The ratio of EPSG and IPSP during SWRs was smaller for PCs than those calculated for interneurons ($p<0.001$), but in interneurons there was no significant difference in this ratio ($p=0.69$). See Table 2 for details.

Figure 5. Comparison of synaptic conductances during SWRs in spiking and non-spiking neurons. A, EPSG during SWRs was similar in spiking and non-spiking pyramidal cells, but spiking interneurons received larger excitation than their non-spiking pairs (open, spiking neurons; dashed, non-spiking neurons, a, $p=0.005$; b, $p=0.03$). Only non-spiking ivy cells were observed ($n=5$). B, IPSP measured during SWRs was significantly smaller in spiking pyramidal cells than in non-spiking ones ($p=0.02$), however, there was no difference in IPSP magnitude in interneurons. C, A camera lucida reconstruction of an ivy cell (dendrites, black; axon, red). Scale bar, 100 μm . D, Larger EPSG to IPSP ratio characterizes spiking than non-spiking cells. This ratio was significantly larger for pyramidal cells (a, $p=0.02$), for CB1+BCs (b, $p=0.008$) and for RAD cells (c, $p=0.048$). EPSG/IPSP ratio for ivy cells was below one. See Table 2 for details.

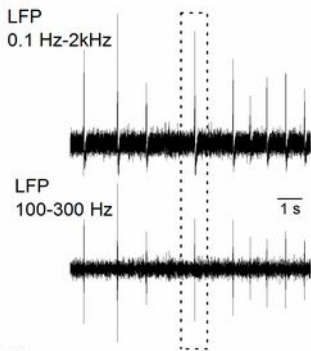
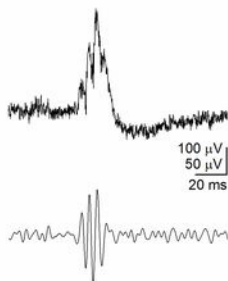
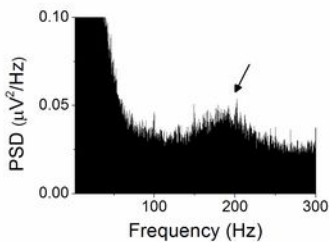
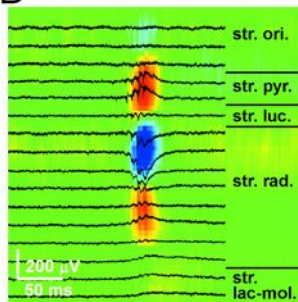
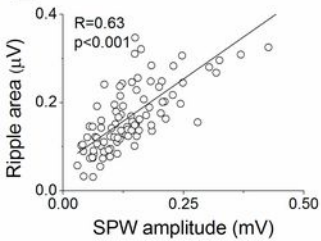
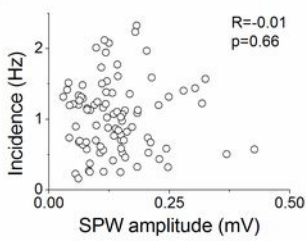
Figure 6. Relationship between the spike number during SWRs and synaptic conductance. A, B, Spike number during SWRs is plotted against excitatory postsynaptic conductance (EPSG) for individual cells. Color coded symbols represent different cell groups. Significant correlation was found between EPSG and the number of spikes during SWRs in interneurons. C, D Spike number during SWRs showed no correlation with inhibitory postsynaptic conductance (IPSP) for pyramidal cells or interneurons. E, F, Spike number during SWRs plotted against EPSG/IPSP ratio showed positive correlation in interneurons, but not in pyramidal cells. In B, F, least-square fit lines are shown.

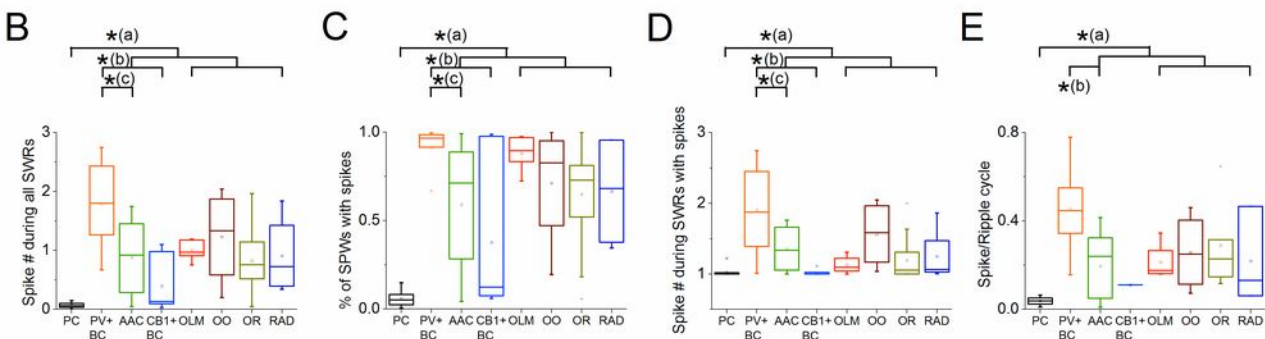
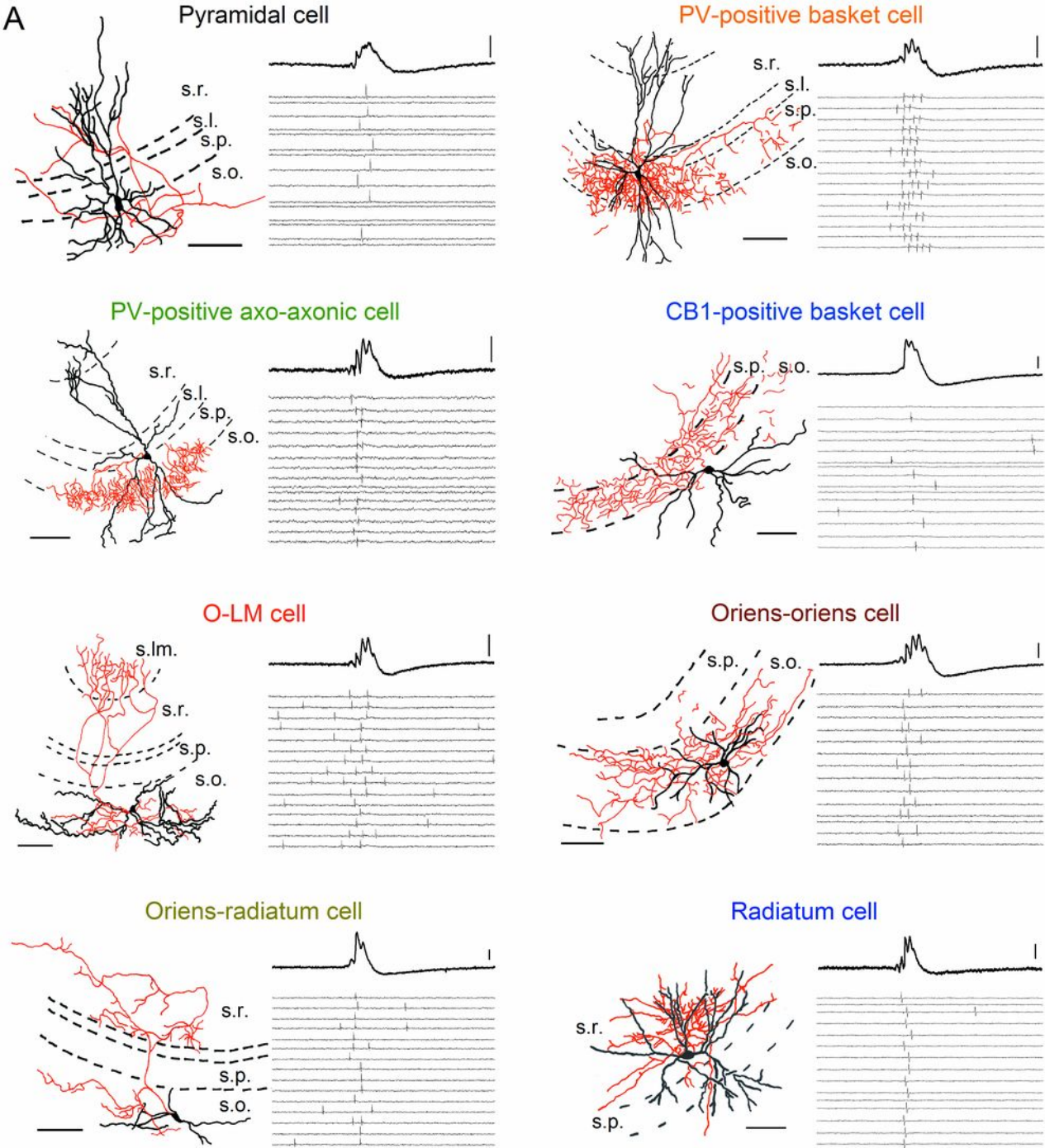
Figure 7. Temporal structure of synaptic inputs relative to the SWR peak. A, A spike distribution histogram, averaged EPSC and IPSC recorded in a PV+ basket cell aligned to the SWR peak illustrates the method used to estimate the temporal structure of synaptic inputs

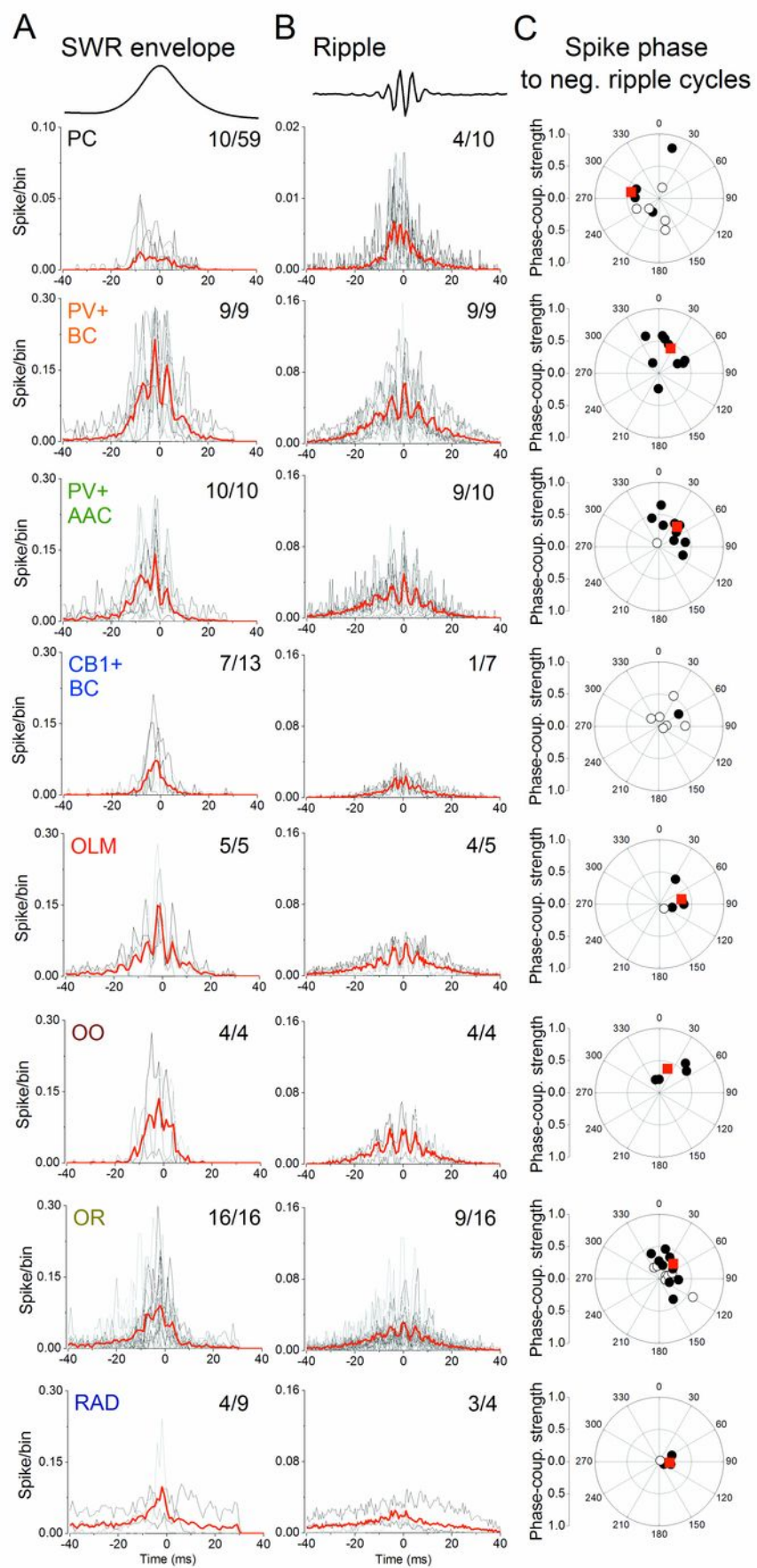
and its correlation to spiking. B, Pre/Post SWR Peak EPSG showed a weak, but significant correlation with the asymmetry in spike distribution histograms, indicating that asymmetry in excitatory input may, at least in part, account for the observed asymmetry in firing relative to the SWR peak. EPSG before the SWR peak (Pre SWR Peak) (C), EPSG after the SWR peak (Post SWR peak) (D), IPSP before the SWR peak (Pre SWR Peak) (E) and IPSP after the SWR peak (Post SWR peak) (F) for distinct cell types with similar dendritic arborization are shown. C, D, PV+BCs receive significantly larger EPSGs both before (* PC vs. PV+BC, $p<0.001$; PV+ BC vs. AAC, $p=0.014$; PV+ BC cell vs. CB1+ BC, $p<0.001$;) and after SWR peak (* PC vs. PV+BC, $p<0.001$; PV+ BC vs. AAC, $p=0.01$; PV+ BC vs. CB1+ BC, $p=0.008$) compared to other cell types, while EPSGs in AACs are larger only before the SWR peak compared to pyramidal cells or CB1+ BCs (# PC vs. AAC, $p=0.006$; AAC vs. CB1+ BC, $p=0.02$). G, The ratios of EPSG before and after the SWR peak in AACs were significantly larger than in other cells types (* PC vs. AAC, $p<0.001$; PV+ BC vs. AAC, $p=0.008$; AAC vs. CB1+ BC, $p<0.001$), while no difference was observed in the ratios of IPSP before and after the SWR peak (H). EPSG to IPSP ratios before the SWR peak (I) or followed the SWR peak (J) are significantly larger in PV+BCs than in pyramidal cells, AACs or CB1+BCs (I, * PC vs. PV+BC, $p<0.001$; PV+ BC vs. AAC, $p=0.001$; PV+ BC cell vs. CB1+ BC, $p<0.001$; J * PC vs. PV+BC, $p<0.001$; PV+ BC vs. AAC, $p=0.001$; PV+ BC cell vs. CB1+ BC, $p=0.026$). See Table 3 for details.

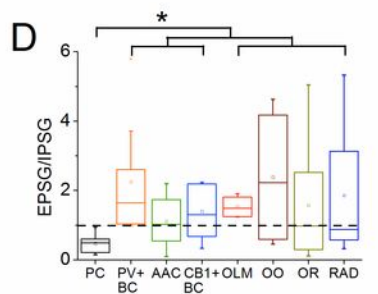
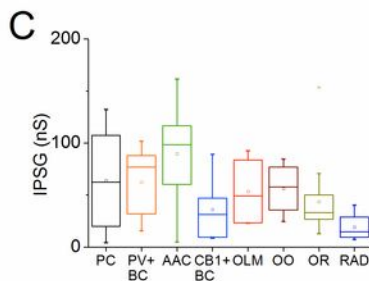
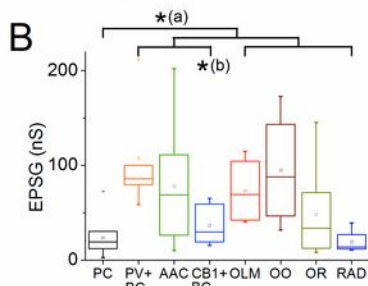
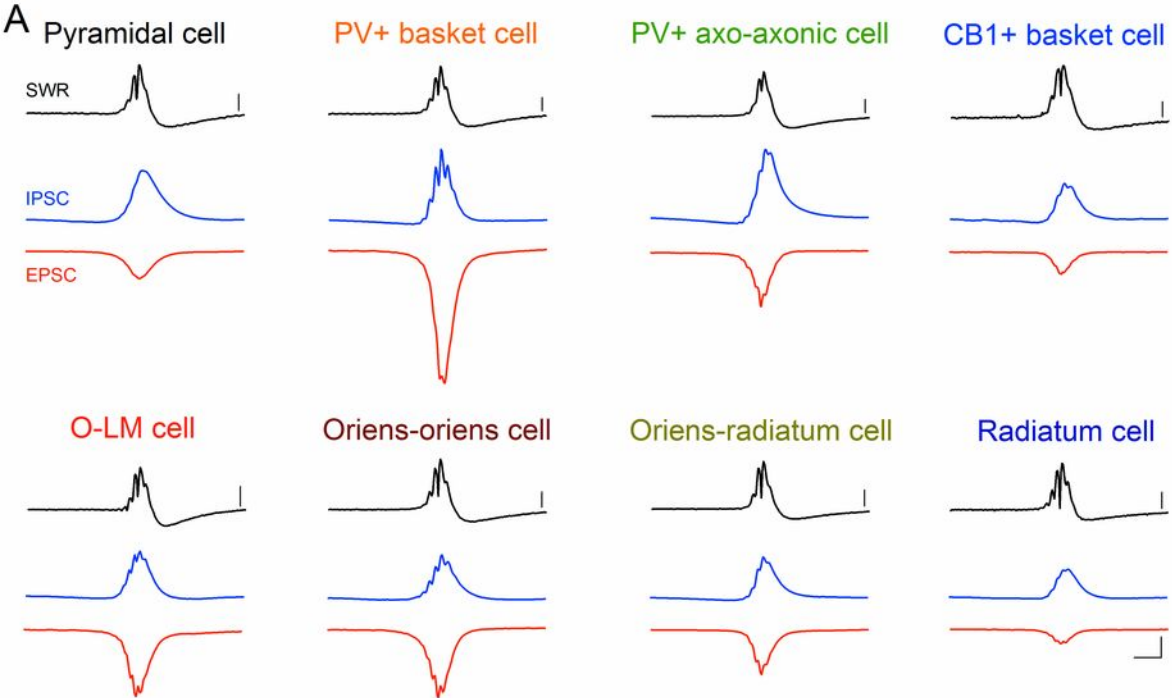
Figure 8. Interaction between excitatory and inhibitory synaptic conductances during SWRs. For a PV+BC (A) and an AAC (B), the net apparent synaptic reversal potential (E_{app} in color) and the spike distribution histogram during SWRs is overlaid (black). The maximums and the minimums of the spike distribution histograms are tightly coupled to the peaks and the troughs in the 'ripple'-like appearance of E_{app} , respectively, indicating that the excitatory and inhibitory synaptic conductances shape together the firing of these interneurons during SWRs. In addition, the asymmetry in the spike distribution histograms relative to the sharp wave peak matches the asymmetry in E_{app} . Top, SWR averages are shown. C, Averaged E_{app} curves calculated only for neurons spiking during SWRs show cell-type specific appearance. E_{app} in the majority of neuron types reaches its maximum before or around the peak of the sharp waves, followed by the sharp drop toward more negative values. However, E_{app} for PV+BCs

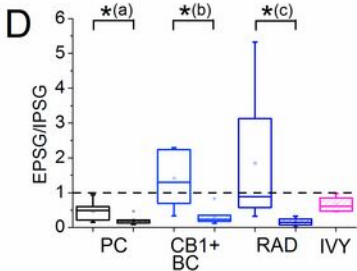
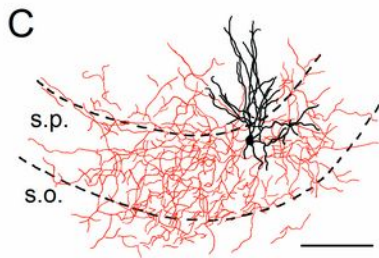
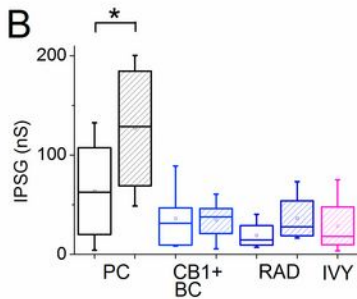
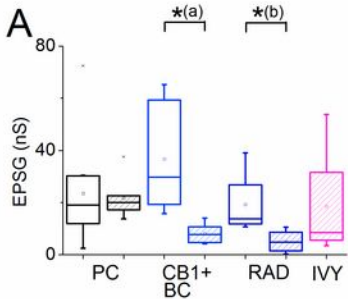
and OLM cells, is more symmetric relative to the sharp wave peak unlike E_{syn}^{peak} for other cell types. Curves are the averages of E_{syn}^{peak} obtained in individual cells. D, Relationship between the peak of E_{syn}^{peak} and the number of spikes during SWRs in different cell classes indicates that more spikes are emitted by those neuron types, in which the peak of E_{syn}^{peak} approaches closer the reversal potential of the synaptic excitation. Error bars indicate SEM. E, F, Asymmetry in E_{syn}^{peak} shows significant correlation with the asymmetry in spike distribution histograms for interneurons (F), but not for pyramidal cells (E).

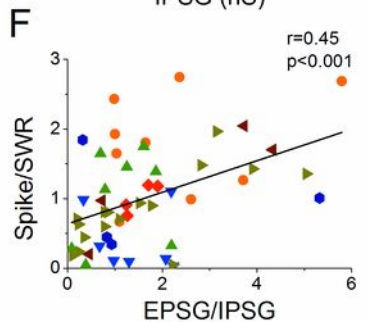
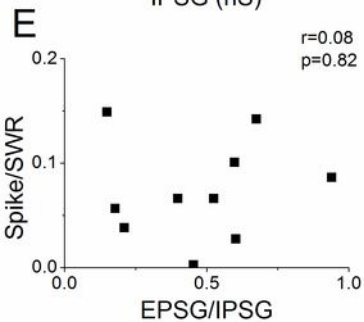
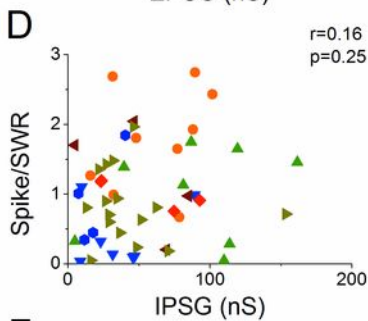
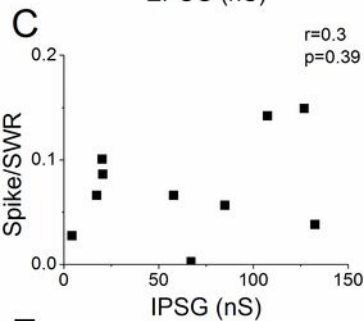
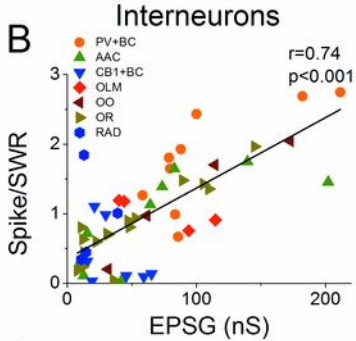
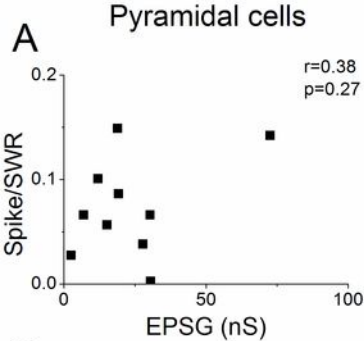
A**B****C****D****E****F**

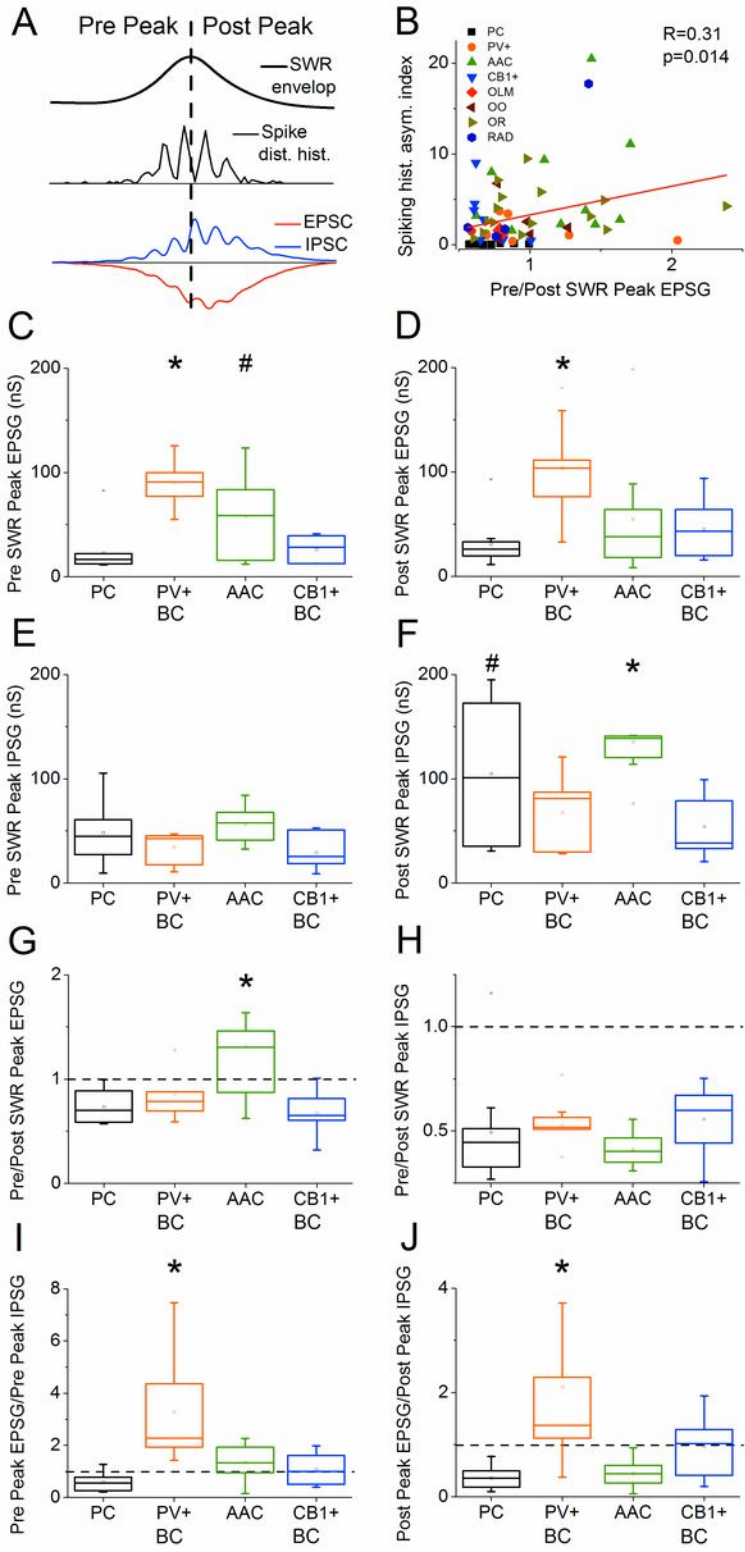












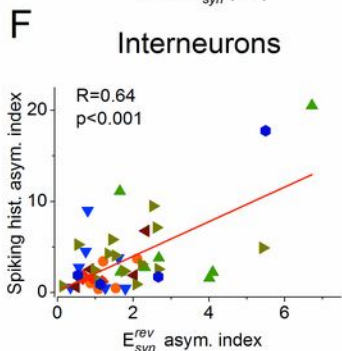
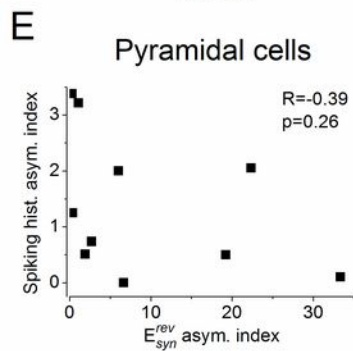
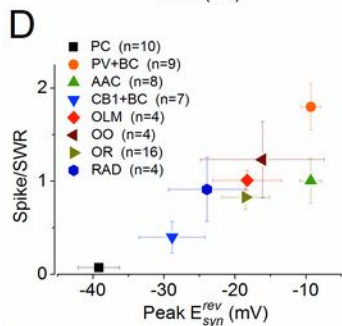
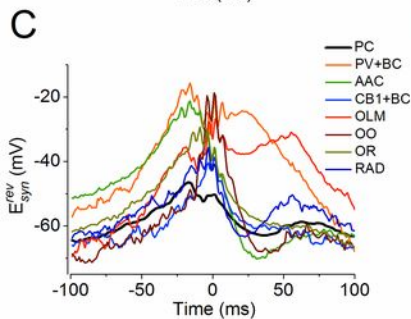
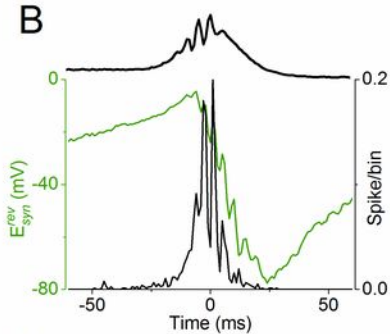
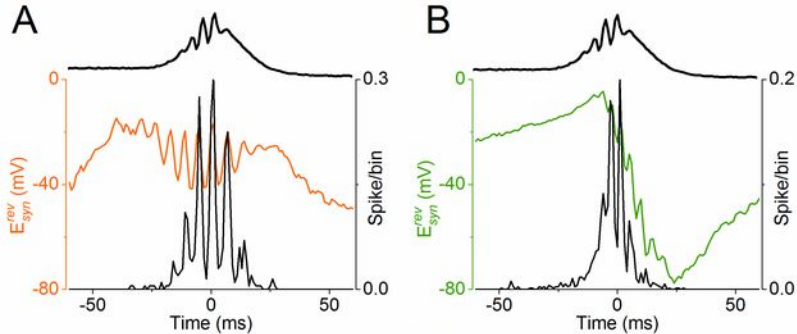


Table 1. Spiking properties of distinct types of anatomically-identified neurons during SWRs.Data are presented as mean \pm SEM.

	PC	PV+ BC	AAC	CB1+ BC	OLM	OO	OR	RAD
	All cells							
	n=10	n=9	n=10	n=7	n=5	n=4	n=16	n=4
Firing Rate between SWRs (Hz)	0.03 \pm 0.01	3.24 \pm 1.88	2.91 \pm 1.12	0.66 \pm 0.41	2.47 \pm 1.17	0.21 \pm 0.09	4.59 \pm 1.01	15.42 \pm 10.61
Firing Rate during SWRs (Hz)	0.49 \pm 0.11	81.52 \pm 16.89	45.11 \pm 11.17	14.98 \pm 5.29	38.87 \pm 12.24	35.93 \pm 13.26	40.34 \pm 7.21	30.32 \pm 15.98
Spike # during all SWRs	0.07 \pm 0.01	1.8 \pm 0.24	0.89 \pm 0.21	0.39 \pm 0.17	1.0 \pm 0.08	1.23 \pm 0.41	0.83 \pm 0.13	0.91 \pm 0.34
Ratio of SWRs with spikes	0.062 \pm 0.016	0.913 \pm 0.038	0.592 \pm 0.117	0.378 \pm 0.159	0.881 \pm 0.047	0.713 \pm 0.179	0.649 \pm 0.071	0.667 \pm 0.167
Spike # during SWRs with spikes	1.03 \pm 0.02	1.91 \pm 0.21	1.35 \pm 0.09	1.02 \pm 0.02	1.13 \pm 0.06	1.57 \pm 0.24	1.19 \pm 0.07	1.25 \pm 0.2
Asymmetry index of spike distribution histograms	0.07 \pm 0.01	1.52 \pm 0.4	6.47 \pm 1.88	3.08 \pm 1.17	1.52 \pm 0.13	2.58 \pm 1.09	3.73 \pm 0.64	5.56 \pm 4.06
	Cells with phase-coupled firing							
	n=4	n=9	n=9	n=1	n=4	n=4	n=9	n=3
Spike /Ripple Cycle	0.038 \pm 0.01	0.455 \pm 0.061	0.196 \pm 0.052	0.111	0.214 \pm 0.044	0.26 \pm 0.088	0.29 \pm 0.065	0.219 \pm 0.125
Spike Time (ms)	-4.25 \pm 2.53	0.52 \pm 0.79	-1.12 \pm 0.69	0.16	1.32 \pm 0.78	1.11 \pm 1.79	2.31 \pm 0.48	0.97 \pm 2.38
Phase ($^{\circ}$) \pm Circular SD	282.5 \pm 63.5	25.3 \pm 56.5	42.4 \pm 37.8	58.7	77.3 \pm 27.2	18.3 \pm 29.3	42.8 \pm 54.8	95.2 \pm 23.3
Length of Mean Vector	0.45 \pm 0.12	0.42 \pm 0.05	0.42 \pm 0.04	0.36	0.39 \pm 0.03	0.39 \pm 0.11	0.32 \pm 0.03	0.16 \pm 0.04

Table 2. Properties of synaptic inputs recorded in distinct types of neurons during SWRs. Data are presented as mean \pm SEM.

	PC	PV+ BC	AAC	CB1+ BC	OLM	OO	OR	RAD
	active cells during SWRs							
	n=10	n=9	n=8	n=7	n=4	n=4	n=16	n=4
EPSP during SWRs (nS)	23.5 \pm 6.2	107.5 \pm 17.4	78.1 \pm 23.1	36.5 \pm 7.6	73.2 \pm 18.5	94.9 \pm 31.1	48.4 \pm 10.5	19.3 \pm 6.6
IPSP during SWRs (nS)	63.8 \pm 15.1	62.4 \pm 10.3	89.6 \pm 17.3	36.3 \pm 10.5	53.5 \pm 17.8	56.2 \pm 13.1	43.6 \pm 8.3	19.2 \pm 7.3
EPSP/IPSP during SWRs	0.47 \pm 0.08	2.25 \pm 0.54	1.11 \pm 0.26	1.39 \pm 0.29	1.53 \pm 0.16	2.38 \pm 1.06	1.57 \pm 0.37	1.85 \pm 1.16
	silent cells during SWRs							
	n=7	n=0	n=0	n=6	n=0	n=0	n=0	n=4
EPSP during SWRs (nS)	21.7 \pm 2.9	NA	NA	8.2 \pm 1.6	NA	NA	NA	5.1 \pm 2.3
IPSP during SWRs (nS)	127.3 \pm 21.6	NA	NA	34.8 \pm 7.9	NA	NA	NA	36.4 \pm 12.8
EPSP/IPSP during SWRs	0.21 \pm 0.04	NA	NA	0.32 \pm 0.11	NA	NA	NA	0.16 \pm 0.06

Table 3. Properties of synaptic inputs before and after the peak of sharp wave envelop in distinct types of neurons during SWRs. Data are presented as mean \pm SEM. Bold indicate the significant differences.

	PC	PV+ BC	AAC	CB1+ BC	OLM	OO	OR	RAD
	n=10	n=9	n=8	n=7	n=4	n=4	n=16	n=4
Pre Peak EPSC (nS) ^a	23.1 \pm 6.7	90.2 \pm 8.1	58.3 \pm 12.2	26.3 \pm 4.4	66.4 \pm 15.5	66.6 \pm 15.5	40.9 \pm 7.7	16.6 \pm 2.8
Post Peak EPSC (nS) ^b	31.1 \pm 7.3	104.1 \pm 15.0	55.1 \pm 17.8	45.5 \pm 10.9	87.9 \pm 19.5	75.8 \pm 21.7	41.2 \pm 7.4	22.9 \pm 8.1
Pre Peak IPSC (nS)	48.4 \pm 9.9	34.5 \pm 4.9	56.4 \pm 6.2	29.3 \pm 6.3	39.9 \pm 11.0	51.4 \pm 10.6	28.2 \pm 3.1	15.1 \pm 1.7
Post Peak IPSC (nS) ^c	104.9 \pm 20.3	67.6 \pm 11.0	135.8 \pm 13.2	54.3 \pm 10.9	66.2 \pm 13.9	87.1 \pm 20.1	65.2 \pm 12.3	33.4 \pm 6.6
Pre/Post Peak EPSC ^d	0.73 \pm 0.05	0.86 \pm 0.08	1.32 \pm 0.18	0.67 \pm 0.08	0.74 \pm 0.05	0.95 \pm 0.12	1.06 \pm 0.11	0.88 \pm 0.19
Pre/Post Peak IPSC	0.49 \pm 0.08	0.53 \pm 0.04	0.41 \pm 0.03	0.56 \pm 0.06	0.62 \pm 0.11	0.60 \pm 0.03	0.48 \pm 0.03	0.49 \pm 0.07
Pre Peak E/IPSC ^e	0.59 \pm 0.11	3.27 \pm 0.66	1.35 \pm 0.25	1.09 \pm 0.22	1.71 \pm 0.12	1.74 \pm 0.8	1.81 \pm 0.4	1.19 \pm 0.33
Post Peak E/IPSC ^f	0.36 \pm 0.06	2.11 \pm 0.59	0.45 \pm 0.09	0.97 \pm 0.22	1.41 \pm 0.24	1.13 \pm 0.5	0.87 \pm 0.2	0.88 \pm 0.48

^a **PC vs. PV+BC, p<0.001; PC vs. AAC, p=0.006; PC vs. CB1+BC, p=0.8; PV+ BC vs. AAC, p=0.014; PV+ BC cell vs. CB1+ BC, p<0.001; AAC vs. CB1+ BC, p=0.02**

^b **PC vs. PV+BC, p<0.001; PC vs. AAC, p=0.2; PC vs. CB1+BC, p=0.7; PV+ BC vs. AAC, p=0.01; PV+ BC vs. CB1+ BC, p=0.008; AAC vs. CB1+ BC, p=0.6**

^c **PC vs. PV+ BC, p=0.08; PC vs. AAC, p=0.15; PC vs. CB1+BC, p=0.02; PV+ BC vs. AAC, p=0.003; PV+ BC vs. CB1+ BC, p=0.56; AAC vs. CB1+ BC, p=0.001**

^d **PC vs. PV+ BC, p=0.44; PC vs. AAC, p<0.001; PC vs. CB1+BC, p=0.71; PV+ BC vs. AAC, p=0.008; PV+ BC vs. CB1+ BC, p=0.29; AAC vs. CB1+ BC, p<0.001**

^e **PC vs. PV+BC, p<0.001; PC vs. AAC, p=0.16; PC vs. CB1+BC, p=0.38; PV+ BC vs. AAC, p=0.001; PV+ BC cell vs. CB1+ BC, p<0.001; AAC vs. CB1+ BC, p=0.66**

^f **PC vs. PV+BC, p<0.001; PC vs. AAC, p=0.85; PC vs. CB1+BC, p=0.21; PV+ BC vs. AAC, p=0.001; PV+ BC cell vs. CB1+ BC, p=0.026; AAC vs. CB1+ BC, p=0.31**